



Doctoral Thesis in Chemical Engineering

Studies on Rechargeable Fe-air electrodes in Alkaline electrolyte

Alagar Raj Paulraj

Doctoral Thesis 2019

KTH Royal Institute of technology

Department of Chemical Engineering

School of Engineering Sciences in Chemistry,
Biotechnology and Health

SE-100 44 Stockholm, Sweden

Studies on rechargeable Fe-air electrodes in alkaline electrolyte

ALAGAR RAJ PAULRAJ

TRITA-CBH-FOU-2019:10

ISBN: 978-91-7873-087-2

Akademisk avhandling som med tillstånd från Kungliga Tekniska Högskolan framläggs till offentlig granskning för avläggande av en teknisk doktorsexamen inom kemiteknik, fredagen den 1 mars 2019 kl 10:00 i Kollegiesallen, Kungl Tekniska Högskolan, Brinellvägen 8, Stockholm.

Fakultetskomponent: Universitetslektor Carlos Ponce de Leon, University of Southampton, United Kingdom.

© Alagar Raj Paulraj, Mars 2019

Tryck: US-AB, Stockholm 2019

Abstract

Energy storage system is an important component in the energy system based on variable renewable energy sources into the grid. Energy storage system could contribute to decarbonization, energy security, offset the demand and supply of the electricity sector, especially for the electric grid. These can be either mechanical, electrochemical, chemical, electromagnetic or thermal devices. The most important functional characteristics of an energy storage system are capital cost, roundtrip efficiency, energy and power rating, response times and cycle life. Electrochemical energy storage systems (EES) have the following edge over the other systems: fast response time, relatively short duration of storage, size, high efficiency, a decentralized installation which is closer to generation or consumption site.

The focus of this thesis is on the development of cost-effective iron anode materials and electrocatalytic air electrodes for Fe-air batteries that potentially could become as an energy storage system. Iron-based systems are attractive due to their safety, cheapness, non-toxicity and ubiquitous availability of materials. However, both the anode and cathode parts have numerous drawbacks that need to be addressed. The anode exhibits poor charge efficiency, rate capability and low capacity utilization while the cathode has sluggish kinetics, poor activity, structural stability and the numbers of active non-noble metal catalysts are limited.

This work utilized Cu and Sn-doped iron nanomaterials and different additives (Bi_2S_3 , CNT, LiOH) to enhance the performance of the iron electrode. The performance of the electrodes were evaluated using the charge/discharge cycling, rate capability, cyclic voltammetry (CV), galvanostatic and potentiodynamic polarization measurements, in operando charging measurements combined with mass spectrometry. The fresh and cycled electrodes and powders were characterized by *ex-situ* XRD, BET, SEM, TEM, XPS and Raman spectroscopy. The most striking results are the prevention of nanoparticle agglomeration, increased charging efficiency (80-91%), effect of Cu and Sn dopants on specific capacity (367-603 mAh g⁻¹) and improved performance of the electrodes at high charge current densities.

In the subsequent air electrode part, non-precious metal La-doped CaMnO_x , nano Co_3O_4 and NiFeO_x electrocatalysts were synthesized using co-precipitation and hydrothermal methods. Both the single and mixed catalysts were used as bi-functional catalysts for oxygen reduction and evolution reactions (ORER). The catalysts were characterized by XRD, SEM, TEM, BET, Raman and XPS. The electrocatalytic activity and stability were assessed in alkaline solutions on gas diffusion electrodes and glassy carbon electrode by linear sweep voltammetry (LSV), CV and rotating disk

electrode (RDE). Furthermore, the mixed catalyst and NiFeO_x showed excellent bifunctional performance such as high activity and stability achieved by the hybridization of the two catalysts and the effect of catalyst loading on the electrocatalytic performance. These findings can help to develop a cost-effective material for Fe-air batteries.

Keywords: Fe-air battery; Cu/Sn-doped nanostructured iron electrodes, Alkaline electrolytes, Bi-functional OER/ORR catalyst, perovskite/spinel catalyst, NiFeO_x , air electrode;

Sammanfattning

Energilagringssystem är en viktig komponent vid integrationen av teknik som genererar el från förnybara energikällor till nätet. Energilagringssystem skulle kunna bidra till avkolning, energisäkerhet, utjämna efterfrågan och utbudet av elsektorn. Energilagringssystem kan vara mekaniska, elektrokemiska, kemiska, elektromagnetiska eller termiska anordningar. De viktigaste funktionella egenskaperna hos ett energilagringssystem är kapitalkostnaden, roundtrip, effektivitet, energi- och effektbedömning, responstider och cyklingsbarhet. De elektrokemiska energilagringssystemen (EES) har följande fördelar över de andra systemen: snabb responstid, relativt kort lagringstid, storlek, hög effektivitet, en decentraliserad installation som ligger närmare generations- eller konsumtionsläge.

Fokus för denna avhandling handlar om utveckling av kostnadseffektiva järnanodmaterial och elektrokatalytiska luftelektroder för Fe-luft batterier som energilagringssystem. Järnbaserade system är attraktiva på grund av deras säkerhet, billighet, icke-toxicitet och allmänt förekommande materialtillgänglighet. Både anoden och katoden har emellertid många nackdelar som behöver åtgärdas. Anoden uppvisar dålig laddningseffektivitet, laddningskapacitet och låg kapacitetsutnyttjande medan katoden har trög kinetik, dålig aktivitet, strukturell instabilitet och val av begränsat antal aktiva icke-ädelmetallkatalysatorer.

Detta arbete utnyttjade Cu- och Sn-dopade järn nanomaterial och olika tillsatser (Bi_2S_3 , CNT, LiOH) för att förbättra järnelektrodens prestanda. Elektrodernas prestanda utvärderades med hjälp av laddnings-/urladdnings cykler, laddningsskapacitet, cyklisk voltammetri (CV), galvanostatisk och potentiodynamisk polarisationsmätningar, in-operando laddnings mätningar kombinerade med masspektrometri. Både nya och cyklade elektroder samt pulver material karakteriserades genom ex-situ XRD, XPS, BET, SEM, TEM och Raman spektroskopi. De mest slående resultaten är förebyggandet av agglomerering av nanopartiklar, ökad laddningseffektivitet (80-91%), effekt av Cu- och Sn-tillsatser på specifik kapacitet ($367\text{-}603 \text{ mAh g}^{-1}$) och förbättrad prestanda hos elektroderna vid hög laddningsströmdensitet.

I den efterföljande delen av denna avhandling av luftelektroder syntetiserades icke-ädel metaller av La-dopade CaMnOx , nano Co_3O_4 och NiFeOx katalysatorer med hjälp av utfällning och hydrotermiska metoder. Både enskilda och blandade katalysatorer användes som bi-funktionella katalysatorer för syrereduktions och evolutions reaktioner (ORER). Katalysatorerna karakteriserades med hjälp av XRD, SEM, TEM, BET, Raman och XPS. Den elektrokatalytiska aktiviteten och stabiliteten analyserades i alkaliska lösningar med gasdiffusionselektroder och

glaselektrod genom linjär svepvoltammetri (LSV), CV och roterande skivelektrod (RDE). Dessutom några avgörande observationer noterades om utmärkt bifunktionell prestanda, såsom aktivitet och stabilitet genom hybridisering av två katalysatorer, samt inverkan av mängden katalysator på den elektrokatalytiska prestandan. Dessa resultat kan bidra till att utveckla ett kostnadseffektivt material för Fe-air batterier.

Nyckelord: Fe-luft batteri; Cu/Sn-dopade nano-strukturerade järnelektroder, Alkalisk elektrolyt, Bi-funktionell OER/ORR-katalysatorer, perovskit/spinel katalysator, NiFeO_x, luftelektrod;

List of appended papers

Paper 1

Core/Shell Structure Nano-Iron/Iron Carbide Electrodes for Rechargeable Alkaline Iron Batteries

Alagar Raj Paulraj, Yohannes Kiros, Björn Skårman, Hilmar Vidarsson

Journal of The Electrochemical Society, 164 (2017), A1665-A1672.

<https://doi.org/10.1149/2.1431707jes>

Paper 2

La_{0.1}Ca_{0.9}MnO₃/Co₃O₄ for oxygen reduction and evolution reactions (ORER) in alkaline electrolyte

Alagar Raj Paulraj, Yohannes Kiros,

Journal of Solid State Electrochemistry 22 (2018), 1697-1710

<https://doi.org/10.1007/s10008-017-3862-2>

Paper 3

Electrochemical Performance and in Operando Charge Efficiency Measurements of Cu/Sn-Doped Nano Iron Electrodes

Alagar Raj Paulraj, Yohannes Kiros, Mylad Chamoun, Henrik Svengren, Dag Noréus, Mats Göthelid, Björn Skårman, Hilmar Vidarsson, Malin B. Johansson

Batteries 5 (2019), 1.

<https://doi.org/10.3390/batteries5010001>

Paper 4

NiFeO_x as a bifunctional electrocatalyst for oxygen reduction (OR) and evolution (OE) reaction in alkaline media

Alagar Raj Paulraj, Yohannes Kiros, Mats Göthelid, Malin Johansson
Catalysts 8 (2018), 328.

<https://doi.org/10.3390/catal8080328>

Papers not included in the thesis

Paper 1

Anionic redox chemistry in Na-rich $\text{Na}_2\text{Ru}_{1-y}\text{Sn}_y\text{O}_3$ positive electrode material for Na-ion batteries

Patrick Rozier, Mariyappan Sathiya, Alagar-Raj Paulraj, Dominique Foix, Thomas Desautay, Pierre-Louis Taberna, Patrice Simon, Jean-Marie Tarascon

Electrochemistry Communications 53 (2015), 29–32

<https://doi.org/10.1016/j.elecom.2015.02.001>

Paper 2

Radiation-induced synthesis of nanoscale Co- and Ni-based electrocatalysts on carbon for the oxygen reduction reaction

Inna L Soroka, Nadezda V Tarakina, Anton Hermansson, Lukas Bigum, Rickard Widerberg, Mikael S Andersson, Roland Mathieu, Alagar R Paulraj, Yohannes Kiros.

Dalton Trans., 46 (2017), 9995–10002.

<https://doi.org/10.1039/c7dt01162h> rsc.li/dalton

Conference presentations based on this thesis

- I. Electrochemical Study of Nano-Iron/Iron Carbide as Rechargeable Electrodes
Alagar Raj Paulraj, Yohannes Kiros, Björn Skårman, Hilmar Vidarsson
Abstract #96 in the PriME 2016 230nd ECS International Meeting, Honolulu, Hawaii, 2016

- II. Bifunctional Spinel NiFe_2O_4 Electrocatalyst for Oxygen Reduction (OR) and Evolution (OE) in Alkaline Media
Alagar Raj Paulraj, Yohannes Kiros,
Abstract #83 in the 232nd ECS International Meeting, National Harbor, MD, 2017

- III. Capacity Limited Cycle Life of Cu/Sn Doped Nano-Iron/Carbon Electrodes in Alkaline Electrolyte
Alagar Raj Paulraj, Yohannes Kiros, Björn Skårman, Hilmar Vidarsson
Abstract #2062 in the AiMES 2018 234th ECS International Meeting, Cancun, Mexico, 2018 |

Author's contributions to the appended publications

Paper 1: I performed all the experimental work, analyzed the data and wrote the article with guidance of the co-authors.

Paper 2: I performed all the experimental work, analyzed the data and wrote the article with guidance of the co-author.

Paper 3: I am the principal author. Major part of the experiments was conducted and written by me. Henrik Svengren designed the insitu electrochemical GC-MS set-up. Mylad Chamoun carried out the experiments and wrote that part. XPS and Raman analyses were performed and analyzed by Mats Göthelid and Malin B. Johansson. The article was reviewed by all co- authors.

Paper 1: I am the principal author. I performed all the experiments except XPS and Raman, which were performed and analyzed by Mats Göthelid and Malin B. Johansson. I wrote the whole article and it was reviewed by all co- authors.

CONTENTS

1	INTRODUCTION	3
1.1	Need of energy storage.....	3
1.2	Battery systems.....	4
1.3	Iron electrodes for alkaline systems	8
1.3.1	Electrochemistry of the Iron electrode	9
1.3.2	Challenges in the iron electrode	11
1.3.3	Overcoming Strategies	11
1.4	Bifunctional catalysts for ORR and OER in alkaline metal-air batteries	13
1.4.1	Non-noble metal catalysts	13
1.4.2	Electrochemical reactions at the positive electrodes	17
1.5	Scope of the thesis	19
2	EXPERIMENTAL METHODS	23
2.1	Materials synthesis and electrode preparation.....	23
2.1.1	Iron negative electrodes.....	23
2.1.2	Oxygen electrode materials	25
2.1.3	Composite air electrode preparation	27
2.1.4	Physical characterization	28
2.1.5	Electrochemical measurements	30
2.1.6	Air electrode testing	32
3	RESULTS AND DISCUSSION	37
3.1	Phase identification of the Cu and Sn doped iron samples.....	37
3.2	Surface and porosity of Cu and Sn doped iron samples	39
3.3	Morphology of the Cu and Sn doped iron samples	41
3.4	Analysis of surface oxidation state and species of Cu doped iron sample	42

3.5	Electroanalytical Characterization of Cu and Sn doped iron sample	44
3.5.1	Cyclic voltammetry of Cu doped iron	44
3.5.2	Cyclic voltammetry of Cu, CuSn and Sn doped iron.....	46
3.5.3	Electrode kinetics	47
3.6	Galvanostatic cycling of Cu, CuSn, and Sn-doped iron electrodes	49
3.6.1	Cu-doped iron electrodes cycling performance	49
3.6.2	CuSn and Sn-doped iron electrodes cycling performance	54
3.6.3	Effect of charge current density on hydrogen evolution and electrode performance on Cu, CuSn, and Sn-doped iron electrodes	56
3.7	Galvanostatic cycling effect on Cu-doped electrode	60
3.7.1	Impedance evolution along the galvanostatic cycling	60
3.7.2	Ex-situ XRD phase evolution	62
3.7.3	Ex-situ morphological evolution	63
4	ELECTROCATALYTIC STUDIES ON MIXED-OXIDE LA-DOPED CAMNO_x AND CO₃O₄ CATALYSTS AND NIFE_xO_x.....	67
4.1	Phase identification of synthesized particles	67
4.2	Surface area characterization	68
4.3	Morphological characterization	69
4.4	Surface species characterization	71
4.5	Electrochemical identification of redox activity	72
4.5.1	Cyclic voltammetry	72
4.6	Electrode kinetics	75
4.6.1	Initial stage of the electrocatalytic activity	75
4.6.2	Tafel characteristics	78
4.7	ORR activity	80
4.8	Bifunctional OER and ORR cycling	83
4.8.1	Bifunctional stability of LCMO and Co ₃ O ₄ based electrodes.....	83
4.8.2	Bifunctional stability of NiFeO _x based electrodes.....	86

4.9	Mass activity comparison between GC vs. GDE composite electrodes of LCMO+Co ₃ O ₄	88
4.10	Postmortem analysis of LCMO and Co ₃ O ₄ cycled electrodes	89
5	CONCLUSION AND OUTLOOK.....	95
6	ACKNOWLEDGMENT	98
7	REFERENCES.....	99

PART I: INTRODUCTION

PART I

1 Introduction

1.1 Need of energy storage

Electricity is an important energy carrier that maintains our comfortable way of life. Currently two-thirds of the energy we consume comes from fossil fuels. Various national government agencies, like the US Department of Energy (DOE), and international energy agencies, predict that this scenario will continue until 2040, with 54% of energy coming from fossil fuels and 33% coming from renewables (hydro, solar, wind and geothermal power)¹. Ongoing fossil fuel usage has contributed to the rise of CO₂ concentrations above 410 ppmv (parts per million by volume). This trend will also continue until 2040. Electricity generation alone contributes 25% of GHG². This causes a significant global warming effect. The 2015 Paris Agreement aims limiting global temperature level changes to not extending 2°C above pre-industrial levels by 2100. To achieve this target, carbon-neutral energy production from renewables needs to account for 60% of total electricity production¹. Renewables are the way to offset fossil-fuel-induced global warming.

Therefore, sustainability and environmental awareness have motivated us to diversify our energy sources to include more renewable ones. The energy generation from renewable sources has increased at a remarkable rate since the end of the 1990s. It is expected to increase from 2112 GW in 2016 to 3733 GW by 2040, with a growth rate of 2.3% per year. Solar and wind energy increased by 17% and 25% from 2015 to 2016, with a total installed capacity of 227.1 and 432.9 GW, respectively Global Wind Energy Council, Global Wind 2015 Report: Annual Market Update³. However, their intermittent nature requires large-scale energy storage systems (EES) to store and distribute the energy on demand. Like electricity generation, EES options are highly diverse, nevertheless must have

the following properties: scalability, low life-cycle cost, high current efficiency and a fast response time for withdrawal from the system⁴. EES systems have multiple functions and requirements, such as meeting the unreliable demands of electricity, distributed energy storage, maintenance, utilization, load balance, peak shaving, leveling and stabilizing, and providing an uninterrupted power supply with frequency and voltage control of transmission and distribution to the electricity grid. EES are a vital and indispensable technology for both utility and transmission applications⁵⁻¹⁰.

Energy can be stored in chemical, mechanical, electrochemical, electrical, and thermal forms. Among these, the mechanical form of energy storage, through pumped hydroelectric storage, composed 96% of the total globally installed capacity of EES in 2016. Of the remainder, 2% was in thermal storage and 0.9 % was in electrochemical storage¹. The main advantage of the pumped hydroelectric storage is its low capital cost compared to other available storage solutions (\$80-200/kWh)^{11, 12}. However, this system is site centric and located in ecologically sensitive zones, which means it affects the site's flora and fauna. On the other hand, electrochemical energy storage systems, like batteries, are flexible in design scale and size, have a low response time, a high round-trip efficiency, and can be built in any location. They also come in several different storage formats, including secondary batteries, supercapacitors, and redox flow batteries. Each type of electrochemical system can change significantly, based on energy and power densities, charge and discharge duration, cycling behavior, and capital cost.

1.2 Battery systems

Batteries are devices that store electrical energy at their anode and cathode electrodes in the form of chemical energy; in the electrolyte medium-charged ions and along the external circuit electrons move. Two chemical reactions take place at the same time in the electrode/electrolyte interphase: on discharge at the anode (negative electrode), oxidation occurs, and at the cathode (positive electrode), reduction occurs. During charging, the reverse of these reactions

takes place. From the application point of view, energy delivered during the discharge should be as high as possible. This output energy is directly related to the amount of active material in the battery. The total amount of energy stored in the battery is called specific energy (Wh/kg), and the speed at which it can be extracted from the system is defined as specific power (W/kg). The other important parameter is round-trip efficiency, in which minimum loss signifies an efficient system with less energy waste. The weight and volume of the system also play an important role in the application. Several applications, such as automotive and traction, will require high power density, while at grid level, large-scale energy storage applications need high energy density batteries with no weight limitations. However, a higher rate of withdrawal tends to decrease the energy density by the Joule heating effect. For the efficient utilization of the battery, the optimum value of the power and energy density needs to be fixed. When the battery is not in use, valuable energy is lost in an unwanted reaction called self-discharge; this needs to be minimized for effective storage and must be most reliably redrawn from the battery into the applications. Mechanical integrity is also an essential criterion because the battery is often subjected to thermal, mechanical and vibrational shocks. Therefore, the desired characteristics are maximum energy at optimum power density, minimum self-discharge, minimum internal resistance, maximum mechanical robustness and long cycle, cost-effectiveness, wide availability and less environmental impact ¹³.

More than a century of research on storage batteries has produced few viable systems. The lead-acid battery, first demonstrated in 1859 by Gaston Planté, is now ubiquitous due to its cost and robustness. The lead-acid system has low energy density (30 Wh/kg), toxic raw material and a low life cycle (300 cycles). Since then, many systems have been developed, such as Ni-Cd, Ni-MH, and Ni-Fe. The performance of Ni-Cd suffers from memory effect, and to resuscitate the lost capacity users have to perform a time-consuming recharging regime. Although the Ni-Cd offers slightly higher energy and a higher life cycle (1500 cycles) than the lead-acid battery, toxicity and a higher self-discharge rate of cadmium

have urged to replace it with metal hydride electrodes (MH). The Ni-MH can store more energy than the Ni-Cd. Even though it delivers less power and is tolerant to overcharge, the high cost of rare earth elements is a drawback. To circumvent the above downsides, the MH electrode has been replaced with an iron electrode, which can provide 1.5 to 2 times more specific energy and life cycle (2000 cycles at 80% DOD) than lead-acid batteries, with increased mechanical robustness^{14, 15}. Overall, iron electrodes are safer, more environmentally friendly and more cost-effective than lead, nickel, zinc, cadmium, and metal hydrides.

This chapter highlights the electrochemical characteristics of the iron electrode in alkaline media. The issues that affect iron electrodes and approaches to tackling those issues are discussed here.

Several systems have been developed in the last 100 years from Ni-based batteries (Ni-MH, Ni-Cd, Ni-Fe, Ni-Zn, NaNiCl₂), redox flow batteries (Vanadium, Zn-Br, Zn-Cl, Zn-Ce, Fe-Cr, V-Br), NaS and metal-air batteries (Fe-air, Zn-air, Li-air, Al-air and Mg-air)^{9, 10, 16-18}. The later type of battery is used in a wide range of applications due to a combination of anodes from batteries and air cathodes from fuel cells, which give them high energy and power density, better safety and environmental viability. Fe-air, Zn-air, Mg-air, Al-air, and Li-air have a theoretical energy density of 1129, 1353, 6815, 8076 and 11429 Wh kg⁻¹¹⁹. Each system has its own set of merits and demerits. Even though Al, Mg, Zn, and Li negative electrodes have a higher theoretical energy density than Fe, the inherent drawbacks of these metal electrodes are dendrite formation, uneven metal deposition, corrosion of metal anode and reactivity/dissolution, posing a severe challenge to widespread commercialization. Furthermore, they are costlier than the Fe-based systems. Iron is the fourth most abundant element in the Earth's crust (known reserves are 230×10⁹ tons); it is the most available, least expensive and least toxic element to be used for large-scale battery energy storage systems US Geological Survey, Mineral Commodity Summaries^{20, 21}.

The air cathode as a positive electrode is widely used in various electrochemical systems such as metal-air batteries, metal hydride-air batteries, regenerative fuel cells, and electrolyzers ²²⁻²⁴. Currently, acidic and alkaline electrolytes are employed in fuel cells and batteries. For metal-air batteries, alkaline electrolytes are favored over acidic due to their higher ionic conductivity, activity, electrode materials corrosion resistance, better safety issues, and sustainable materials (non-precious metals group), compared to organic or acidic electrolytes. Moreover, transition metal oxides are stable and active in an alkaline electrolyte ²⁵. Also, the critical transition metals and rare earth elements Ni, Ca, Fe, and Mn are widely available in the earth's crust. These elements are sustainable. Ca, Fe, Mn are important constituents in the biomass, and are easily recyclable.

The operation of rechargeable Fe-air batteries (Figure 1. 1) is similar to that of the Zn-air battery for the air electrode, which catalyzes both oxygen evolution reaction (OER) and oxygen reduction reaction (ORR) during charge and discharge respectively, while the Fe electrode is oxidized during discharge and reduced back to Fe during charge (Eq 1.1-1.2). There are significant voltage and energy losses during this charge and discharge cycle, both on the metal and air electrode operation. The iron electrode undergoes self-corrosion, parasitic hydrogen evolution and passivation, leading to low utilization and energy efficiency ^{4, 26-28}. On the other hand, the air electrode has sluggish kinetics and activity, carbon support corrosion, and plugging of electrode pore by CO₂ ^{29, 30}. Altogether, the downsides mentioned above impede the commercialization of Fe-air batteries.

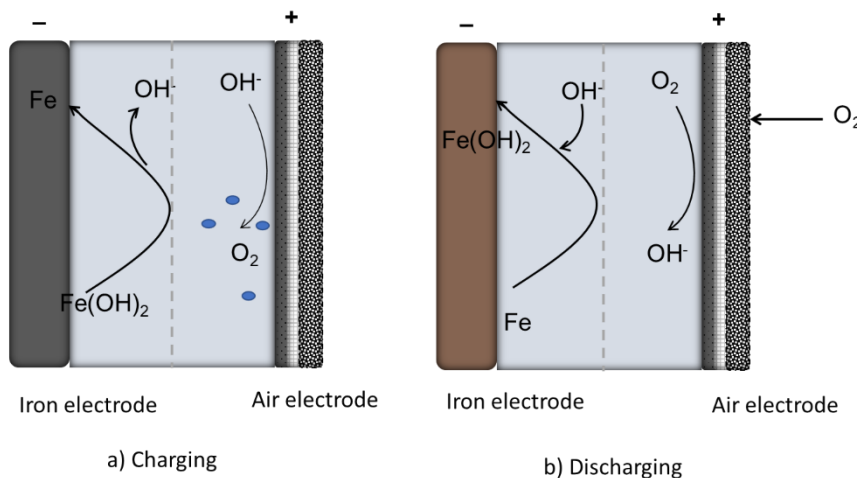
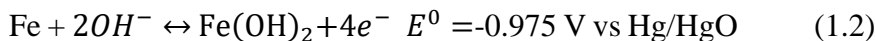
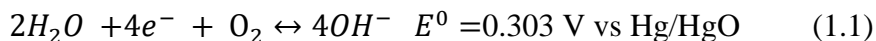


Figure 1.1. Working principle of Fe-air battery³¹



The first part of this work aims to develop a high-capacity negative iron electrode for the Fe-air system. The aim of the second part is to produce active, durable transition metal oxides (CaMnO_x and NiFeO_x, CoO_x) as cathode catalysts for alkaline metal-air batteries, by synthesizing different ways of obtaining the most desired crystal and microstructure as well as incorporating co-catalysts for OER or ORR to enhance the electrode's bi-functional activity and stability.

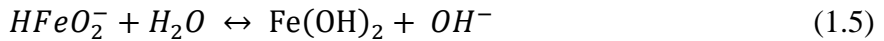
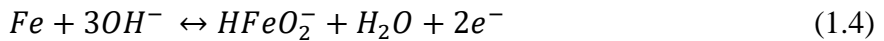
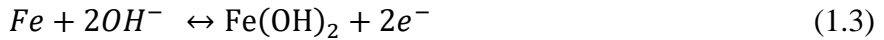
1.3 Iron electrodes for alkaline systems

Iron electrodes are one of the most robust electrodes, working perfectly for about 3000 cycles in a Ni-Fe secondary battery. The electrode reaction products are insoluble in alkaline media, which makes them stable for several cycles in electrode operation. The performance requirements for grid-level storage are: \$100/kWh of

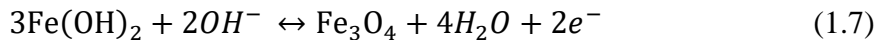
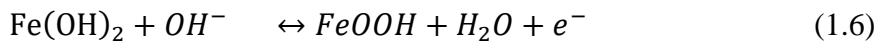
capital cost amortized over a 15-year span, as defined by the US Department of Energy (DOE). A battery life of over 5000 cycles and a round-trip efficiency of 80% are required to meet that target⁴. The Ni-Fe battery's open cell potential is 1.41 V; converting it to Fe-air makes the cell's energy density up to 100% and is less costly. Fe-air life and cost meet the DOE specification. The successful development of iron electrodes could be used as a negative electrode in Fe-air and Ni-Fe alkaline batteries. The Fe-air system is the cheapest, most environmentally friendly, and most robust system of the batteries available^{4, 31}.

1.3.1 Electrochemistry of the Iron electrode

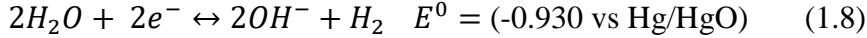
The iron electrode is oxidized in the alkaline electrolyte with oxidation changes from metallic to 2+ then further oxidized into 3+ state. The capacity generating primary reaction is Eq. 1.3^{32, 33}. First, the iron is converted into ferrite ion (Eq. 1.4), This ferrite ion is sparingly soluble, further hydrolyzing and re-precipitate as a hydroxide species (Eq.1.5) on the electrode^{34, 35}. This iron hydroxide is less conductive and passivating the electrode. The thicker layer tends to prohibit the further discharge of the electrode and increase the internal resistance, which intern reduces cell voltage and high rate discharge performance^{21, 27}.



The reactions Eq.1.3 to 1.5 are desired capacity generating reactions in the electrode with a theoretical capacity of 960 mAh g⁻¹³⁶. Further discharge leads iron oxyhydroxide (Eq. 1.6) and magnetite (Eq. 1.7), which require higher overpotential and is hard to reduce into the metallic state³⁷. Also, magnetite is less conductive compared to pure iron. As a consequence, internal resistance of cell increases, resulting in large hysteresis (overpotential) during charging.



Apart from the above reaction, hydrogen evolution is also possible at open circuit potential (OCV) owing to the thermodynamic instability of the iron in the water systems. The standard hydrogen evolution reaction (HER) potential is 40 mV positive to iron electrode's OCV.

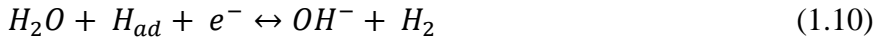


Hydrogen evolution in alkaline electrolyte proceeds in the following pathways: Volmer- Heyrovsky pathway or Tafel path by molecular recombination^{38,39}.

Volmer step:



Heyrovsky step:



Tafel step:



The iron electrode undergoes self-discharge (Eq.1.12) due to the corrosion process, where the reaction scheme is similar to Eq. 1.3 to 1.5. This is partly due to the low thermodynamic hydrogen evolution overpotential causing the hydrogen evolution competing with the iron reduction. These self-discharge rate is as high as 5% per 4 days that could extend it to 20% in a period of 14 days¹⁴.



The concentration gradient of the Fe²⁺ ions causes the iron hydroxide film growth. Thicker film tends to inhibit this self-discharge¹⁴. These self-discharge and hydrogen evolution cause corrosion and waste of energy in the electrode. Therefore, it lowers the faradaic efficiency and water loss of the system. Consequently, overcharging and electrolyte top-up are become mandatory^{21,36}.

1.3.2 Challenges in the iron electrode

To summarize, the problems beset the iron electrode are hydrogen evolution accompanied with low charge efficiency, passivation, low capacity with reduced life, low charge acceptance, low charge retention, poor rate capability.

1.3.3 Overcoming Strategies

The above-mentioned problems are surmounted by modifying the structure, and composition by incorporation of additives into the system, in the electrolyte and electrode, which are added in small quantities to impart specific function. There are few promising options to suppress the hydrogen evolution: such as additives that raise the overpotential of the iron electrode, electrolyte additives that covers active catalytic site in the electrode/electrolyte interphase, and conductivity additives in order to decrease the electrode resistance by carbon, and metal elements such as Cu, Sn, Ni, etc.

1.3.3.1 Electrode additives

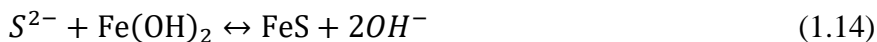
Metal Sulfides and pore formers

A wide range of metal sulfides like FeS, PbS, CuS, NiS, and Bi₂S₃, FeS, Bi₂S₃, Bi₂O₃+K₂S have been utilized as electrode additives. Some of them were discounted in consideration of cost and toxicity. Commonly used pore formers are metal sulfide, nickel sulfate, and potassium carbonate ⁴⁰.

In the electrode, pore formers are used to create enough electrolyte access to the reaction site. Nickel sulfate and potassium carbonate are used in very low concentration (0.5% of active material) and are leached out to the electrolyte forming the pore.

Bismuth sulfide decomposes in a redox reaction, being absorbed into the oxide lattice at the electrode-electrolyte interface. Iron sulfate conductivity is higher than magnetite and iron hydroxide. In the following reactions, 1.13 and 1.14 show bismuth sulfide decomposes by forming iron sulfide. Iron sulfide enables a high discharge rate via de-passivating the oxide; modifying the electrode kinetics and increasing the solubility of iron hydroxide making the

reaction fast. The metallic bismuth increases the hydrogen evolution overpotential and, in addition, charging efficiency increases from 50% to 90% ²¹.



1.3.3.2 Electrolyte additive

Most often, Na₂S, K₂S and LiOH are used as electrolyte additives. The first two function similar to bismuth sulfide, but are less effective due to non-uniformity of sulfide adsorption in the electrode interface. Recently, organosulfur (n-alkanethiols) compounds were successfully used to suppress the hydrogen evolution. Their performance is on par with metal sulfide. Sulfur adsorption masks the electrocatalytic surface site and stays stable over several cycles. The main advantage of using organosulfur is that recycling the used electrode is easy to be compared to a bismuth-containing one ²¹. LiOH increases the use of iron materials by Li ions incorporated into the iron hydroxide matrix, by increasing the ionic conductivity. The intercalated compound also easily reduced back to iron ^{41, 42}.

1.3.3.3 Carbon additive

The discharge products (iron hydroxides) of iron electrodes are insulating and can passivate the electrodes, which prevents further oxidation. The electrode passivation and low material use are overcome by using nano iron and nano iron-carbon composites and FeS materials ⁴³⁻⁵¹. Particularly, iron-carbon additives, such as graphene, MWCNT (multi-wall carbon nano tube), CNF (carbon nano fibre), and amorphous carbon composites showed an increased capacity performance. However, these nanomaterials had a rapid capacity decay. The reason for this is nanoparticle agglomeration and increased hydrogen evolution ⁵²⁻⁵⁶. Sundar Rajan et al. used carbon grafted iron electrodes, which delivered 400 mAh g⁻¹ of capacity at a 100 mA g⁻¹ discharge rate ⁵⁷. Kao et al. reported a high discharge capacity (800 mAh g⁻¹ Fe -Fe ³⁺) at 3200 mA g⁻¹ in the presence of Cu ⁵⁸. The performance results showed that the presence of Cu and amorphous carbon enhances the iron discharge

performance. Chamoun et al. used potassium stannate as an electrolyte additive, which increased the capacity and efficiency to 400 mAh g⁻¹, with 85% charge efficiency⁵⁹. The Sn deposits on the iron electrode are suggested to suppress the H₂ evolution. The reported works show that special carbons, Cu, and Sn have the potential to enhance the iron electrode performance.

1.4 Bifunctional catalysts for ORR and OER in alkaline metal-air batteries

Metal-Air Batteries' (MAB) charging and discharging reactions are oxygen evolution (OER) and oxygen reduction reactions (ORR), which are anodic and cathodic half-cell reactions. These same reactions are a cornerstone of chemical energy to electrical energy conversion, as well as storage and conversion devices including regenerative fuel cells, electrolyzers and photo-electrochemical cells²². However, the OER and ORR reactions are sluggish and require larger overpotential to overcome. This leads to voltage losses that reduce the capacity utilization of the entire metal-air cells. To circumvent this, an active electrocatalyst is vital for the OER and ORR reactions. Alkaline electrolytes used in metal-air batteries offer extra opportunities to enable using both transition metal-based catalysts and noble metal catalysts. The transition metal-based oxides are highly stable and corrosion resistive, which provides an extra advantage to use a wide range of materials in metal-air systems. In this section, perovskite, spinel type nonnoble metal catalysts for bifunctional operations are discussed.

1.4.1 Non-noble metal catalysts

Among the of platinum group metals (PGMs), Pt, Pd, and Pt alloys for ORR and RuO₂ and IrO₂ for OER are considered state-of-the-art electrocatalysts⁶⁰⁻⁶⁴. However, the high cost and limited availability of PGMs and their alloys limits broad-scale commercialization, and they also have poor bifunctional stability. Meanwhile, non-noble metal catalysts such as transition metal oxides of perovskite, layered double hydroxide (LDH), spinels and pyrochlores, are promising due to their structural robustness, bi-functional activity, low cost,

availability and stability in aqueous alkaline electrolytes^{30, 65}. They are thus widely accepted as alternatives for both oxygen reduction (ORR) and oxygen evolution (OER) reactions. In particular, perovskites and spinels are attracted due to the high bifunctional OER and ORR activity and durability and low electrical resistivity. These perovskites and spinels can also use earth abundant transition metals. These can be easily synthesized and provide the morphological flexibility to tune the structure, using the co-precipitation and hydrothermal methods.

1.4.1.1 Perovskites

Perovskites are ABO_3 structure compounds, where A generally belongs to the group of rare-earth divalent ions (La, Ce, Sm, Nd, Gd, Dy, Yd, Ho and Y) or alkaline earth elements (Ca and Sr), while B is a transition metal trivalent ion (Cr, Mn, Fe, Co, Ni, and Cu). La-based perovskites are popular due to their high activity, high oxide ion mobility, mixed ionic and electronic conductivity, and environmental neutrality⁶⁶. Several perovskites have been developed, such as $LaCrO_3$, $LaNiO_3$, $LaMnO_3$, $LaFeO_3$ and $LaCoO_3$ ^{65, 67, 68}. Of these, the Mn and Co-based perovskites have a unique oxidation state and spin configuration that supports stable and high ORER performance. The perovskites' bifunctional OER and ORR activities follow a volcano-type trend. The primary activity descriptor depends on the occupancy of the e_g electronic state; the secondary descriptors are electronegativity and spin state. The preferred e_g electron occupancy for ORR is a less than and for OER it should be greater than one⁶⁹⁻⁷¹. A-site and B-site substitution change the oxidation state and e_g electron filling from less than one to more than one in manganese-based perovskites. Changing the A and B sites produces interesting outcomes, such as increased oxide ion mobility, oxygen non-stoichiometry, and electronic conductivity. This could enhance the electrocatalytic properties to be on par with or even higher than that of PMGs^{72, 73}. Lanthanides and alkaline earth group elements have similar ionic radii. Alkaline earth group elements are easily interchangeable on lanthanum-based perovskites at high-temperature synthesis. This reduces the rare earth element in perovskites and thus reduces the material cost. A

site substitution increases the current density, surface oxygen vacancies, conductivity and stable crystal structure ⁶⁵, while B-site cations tune the bond-forming ability of B to oxygenated species.

Different combinations of perovskites, such as $\text{La}_{1-x}\text{Ca}_x\text{MnO}_3$, CaMnO_3 , and $\text{Ca}_2\text{Mn}_2\text{O}_5$, have been studied ⁷⁴. These have exhibited high oxygen redox activity and was due to the surface oxygen vacancies as additional active sites. The distorted structure of $\text{Ca}_2\text{Mn}_2\text{O}_5$ ($e_g \approx 1$) causes molecular porosity, resulting in high OER performance ⁷⁵. The above results have shown that Ca substitution results in mixed valence of Mn ($e_g < 1$) and oxygen vacancies, resulting in charge compensation that promotes charge transfer and peroxide reduction. The high-porosity $\text{La}_{1-x}\text{Ca}_x\text{MnO}_3$ yielded high conductivity and better bifunctional performance ^{76, 77}. Non-stoichiometric $\text{La}_{0.1}\text{Ca}_{0.9}\text{MnO}_3$, has an increased amount of Mn^{4+} concentration due to Ca substitution; this high-oxidation state provided high conductivity and augmented the ORR performance to be comparable to MnO_2 ⁷⁸⁻⁸⁰. However, as it showed a high ORR performance, its oxygen evolution performance should be improved for better bifunctional operation.

1.4.1.2 Spinel

Spinel (AB_2O_4) are another important type of material with earth-abundant transition metals (Fe, Co, Ni, Cu, and Mn) ⁸¹. Recently, several transition metal oxide spinels and mixed-transition metal oxide spinels have been reported as either bifunctional or single OE or OR electrocatalysts in an alkaline environment; these include cobaltite, ferrites, and manganates. One such spinel, Co_3O_4 , is considered to be an OER electrocatalyst and has also proven to be a magnetic p-type semiconductor with structural stability and a low environmental footprint. As such, it is widely applied in electrochemical energy storage devices such as Li-ion batteries, supercapacitors, solid-state sensors, heterogeneous catalysts, pigments, optical devices, and photocatalysts ^{82, 83}. The mixed valence state in the Co_3O_4 has yielded higher OER activity and stability ⁸⁴⁻⁸⁹. Although its ORR performance is not as good as OER performance, this is due to its low conductivity and surface

interaction. Several works have attempted to improve this performance by using complex or simple processes to prepare the Co_3O_4 with substantial differences in size, shape and surface properties for various applications^{83, 89-94}. Moreover, different co-catalysts have been mixed with Co_3O_4 to achieve high and stable bifunctional activity^{88, 92, 95-97}. Partial substitution on Co_3O_4 tetrahedral sites with Ni, Mn, Cu or Zn has resulted in improved performance. The electronegativity difference between Co and the substitution element tunes the M-O bond, which increases the catalytic properties. The difference in electronegativity of Mn (1.55) and Co (1.80), is believed to alter important role in electron withdrawal and accepting properties^{24, 98-101}. The majority works using manganese and cobalt-based catalysts were reported either alone or with some substitution due to their performance and abundance. MnO_2 -perovskite mixed catalysts have been shown to perform well for bifunctional applications in alkaline electrolyte¹⁰².

1.4.1.3 Layered double hydroxides

Another important class of materials are layered double hydroxides (LDH): these are mixed-valence, ionically conducting solids with a layered structure. LDH phase interlayers are filled with carbonate, nitrate and chloride anions. Their activities are greater than those of the spinel or rock salt-type structures due to their being easily oxidizable to metal hydroxide/oxyhydroxide interphases, which are highly active for the OE reaction⁴⁹. Several LDH phases have performed well on the OER side, such as Ni-Fe, Ni-Co, Co-Fe, Ni-Ni, Ni-Mn, Mn-Co, Co-Mn, and Co-Ni¹⁰³⁻¹⁰⁶. The intercalated anions are easily removable, which results in different oxide or spinel phases with mixed-valency states that provide them with donor-acceptor chemisorption sites for reversible oxygen adsorption¹⁰⁷. In addition, the electron conduction between the mixed valences of the spinel provides high conductivity and dramatically alters the bond strength of surface-intermediate species^{107, 108}. Another important spinel is NiFe_2O_4 , which has attracted significant interest due to its low cost, eco-friendliness, widespread availability, activity, high conductivity, and stability. In both the spinel and LDH phase, the surface-active compounds are metal hydroxide and

oxyhydroxide species with different oxidation states. The synthesizing method and conditions can alter the structure, valence, composition and morphology¹⁰⁹.

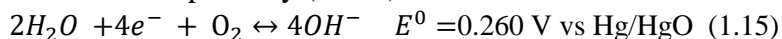
1.4.2 Electrochemical reactions at the positive electrodes

The OER and ORR are the main reactions that govern the Fe-air batteries' charge and discharge operations. As discussed earlier, due to its slow kinetics it needs to be catalyzed by the bifunctional catalyst. The ORR at air electrode involves several steps: oxygen should be brought from atmosphere from the catalyst surface; then it is absorbed on the active site; there is further transfer of electrons from the catalyst to oxygen; then there is a weakening and removal of the oxygen bond; and finally the catalyst surface should release the hydroxide ion to the electrolyte. The OER is exact opposite to the ORR¹¹⁰.

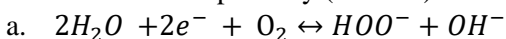
1.4.2.1 Oxygen reduction reaction

The oxygen reduction in alkaline media is proceeded by a series of complex electrochemical reactions. These reactions are mostly dictated by the binding energies from the catalyst to oxygen-containing intermediates (O_2^- , HO_2^- and OH^-). The ORR pathway is given in Table 1.1. Some groups of metals, such as the Pt group, pyrochlore, and perovskite families, favor the direct $4e^-$ pathway, whereas the peroxide path is favored by carbon materials, Hg, Au, most of the transition metals and oxides^{25, 67, 30}. The corrosive peroxide species can oxidize the metal species, damaging the binder and carbon constituents²⁵.

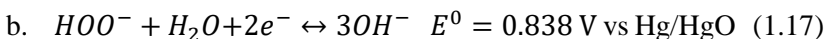
1. Four electron pathway (direct):



2. Two electron pathway (indirect):



$$E^0 = -0.140 \text{ V vs Hg/HgO} \quad (1.16)$$



1.4.2.2 Oxygen evolution reaction

The oxygen evolution mechanism is complex and depends on the multivalence of the metal ions and oxygen intermediaries on the surface. The widely accepted Krasil'shcikov reaction pathways(1.19-1.22) are ¹¹¹.



S is surface active sites. In most cases 4+ oxidation state transition metal acts as a surface-active site, this surface oxidation state is created before the oxygen evolution. Further reaction depends on the surface coverage and rate-determining step ¹¹². In this work the synthesis and characterization of perovskite, spinel and LDH materials as a bifunctional catalyst are presented, further improving the bifunctional performance by mixing the two catalysts to achieve high OER and ORR activities.

1.5 Scope of the thesis

This work aims to explore and develop low-cost iron electrodes and electrocatalytic oxygen electrodes for alkaline Fe-air batteries. Furthermore, different inexpensive materials are synthesized, and their performance mechanisms are investigated. The primary goal is to prepare highly active electrode materials with low environmental impact and easy preparation methods.

The overall goal is to prepare and characterize a robust electrode for a positive and negative electrode for a metal-air battery application. Negative iron electrode materials are studied in papers I and III regarding specific capacity, charge efficiency, life cycles, electrochemical activity and the effect of current density on electrode performances. The air electrode as a positive electrode material, e.g. spinel and perovskite, is studied with regard to electrochemical properties, electrocatalytic performance, stability, and structural stability during and after cycling in papers II and IV.

PART II: EXPERIMENTAL METHODS

PART II Experimental methods

2 Experimental methods

The active materials used in this thesis are Cu and Sn-doped iron-based negative electrode materials, and perovskite ($\text{La}_{1-x}\text{Ca}_x\text{MnO}_3$) and spinel type (CoO_x and NiFeO_x) based oxygen electrode materials. In this section, details about used materials, synthesis, materials characterization methods, electrode manufacturing procedure, and electrochemical characterizations are explained.

2.1 Materials synthesis and electrode preparation

2.1.1 Iron negative electrodes

2.1.1.1 Materials

The iron electrode samples employed in papers 1 and 3 were provided by Höganäs AB. The sample compositions are given in Table 2.1. These elemental compositions are based on differential thermal analysis (DTA) and energy-dispersive X-ray spectroscopy (EDX).

Table 2.1. Iron sample composition

	Electrode	Sample ID	Elemental composition wt. %
Paper 1	2 wt.% Cu	Cu	Cu-2%; carbon-10%; Fe-88%
Paper 3	2 wt.% Cu+ 2 wt.% Sn	CuSn	Cu-2%; Sn-2%; carbon-23%; Fe-73%
	4 wt.% Sn	Sn	Sn-4%; carbon-24 %; Fe-72%

2.1.1.2 Iron electrode preparations

The working electrodes used in papers 1 and 3 were prepared by mixing the nano iron composite (80–85 wt.%), with Ketjenblack–EC-300J (5 wt.%), Bi_2S_3 (5 wt.%) and PTFE 5–10 wt.% (60 wt% in water dispersion, Sigma-Aldrich). In Paper 3, 0.1 wt.% of SWCNT (TUBALL™ SWCNT 0.1 wt.% in NMP solution) was used. The above compositions were homogenized using a high-speed blender at 6000 RPM (Waring® laboratory blender LB20ES), in the presence of D-70 Shellsol®. Then the well-mixed solution was filtered through a 5µm sized filter paper. The retained wet mass was rolled on one side of a 100 mesh nickel screen at 0.7 mm thickness. The pasted electrodes were pressed (375 kg cm^{-2}) and then dried using the stepwise method: first, the solvents from the electrodes were evaporated at 75°C; then at N_2 atmosphere, electrodes were sintered at 325°C for 30 minutes. The average thickness of the sintered electrodes varied between 0.25 and 0.35 mm, depending on the electrode type. The types of electrodes and iron loadings are given in Table 2.2.

Table 2.2. Iron electrode samples

	Electrode	Sample ID	Fe loading (mg cm^{-2})
Paper 1	Cu	Cu	32
Paper 3	CuSn	CuSn	29
	CuSn +0.1 wt.% CNT	CuSnCNT	27
	CuSnCNT	CuSnCNTLi	27
	+0.1 wt.% CNT +0.65 M of LiOH		
	Sn+ 0.1 wt.% CNT	SnCNT	22

2.1.2 Oxygen electrode materials

Electrocatalyst activity highly depends on structure, valence, composition and morphology, and is easily altered by tuning synthesis methods and conditions ¹¹³. By altering the preparation conditions, the electrocatalytic active metal center can be varied to have different crystallinity, phase and crystallite size, and oxidation state ¹⁰⁹.

Traditionally, transition metal oxides are prepared through the conventional solid-state ceramic method, which involves grinding and firing the precursors of carbonates and nitrates at high temperature. While this method is time-consuming and energy-intensive, it only produces a micro-sized wide distribution of nonuniform and low surface area particles, which have poor electrochemical activity ^{114, 115}. Nowadays, there are several other low-temperature routes to produce the nanoparticles by solution-based methods, such as sol-gel, co-precipitation, hydrothermal, iono-thermal, micro-emulsion, microwave, and electrochemical synthesis. Among these several routes, co-precipitation and hydrothermal synthesis are easily scalable, have low-production cost, involve fewer toxic chemicals, have high purity, and homogenous and uniform-sized particles are easily produced ¹¹⁶⁻¹¹⁸.

In this thesis, the carbonate- and hydroxide-assisted co-precipitation method was used in Paper 2 to synthesize perovskite $\text{La}_{0.1}\text{Ca}_{0.9}\text{MnO}_3$ (LCMO) and Co_3O_4 , respectively.

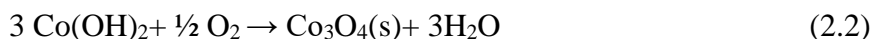
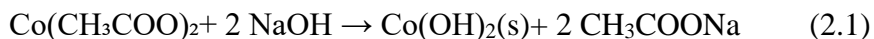
2.1.2.1 Preparation of $\text{La}_{0.1}\text{Ca}_{0.9}\text{MnO}_3$

Here the carbonate-assisted co-precipitation method was used (Paper 2) to prepare the initial carbonate hydroxide product. Then it was heated to get the final desired product. The precursors of Mn, La, Ca (1:0.11:0.9) salts were first dissolved in distilled water. Then to the heated solution (60 °C) was slowly added to the 0.5 M sodium carbonate solution (60 °C) and stirred vigorously. The precipitated product was dried at 120 °C for 12 h. The homogenized product was sintered at 700 °C in air for 6 h and was rapidly quenched in a water-

cooled zone. The resultant final product was washed in 5% acetic acid to remove the unreacted reactant and reduce the strong alkalinity²³.

2.1.2.2 Preparation of Co₃O₄

The hydroxide-mediated co-precipitation method was employed (Paper 2) to get the spinel cobalt oxide. The cobalt acetate tetrahydrate (9.66 g-VWR chemicals) was solubilized in 200 ml of methanol ($\geq 99.8\%$, SIGMA-ALDRICH). The solution was heated and stirred in a two-necked 0.5 L flat-bottom flask at below 65 °C. Another 200 ml of deionized water and isopropyl alcohol (1:1) was added, and the solution temperature was raised to 90 °C with a vigorous mixing by magnetic stirring. To avoid evaporation, a reflux condenser was connected to the two-necked flask. Then 1 M NaOH (100 ml) was added to the cobalt ion solution. The solution transformed from pink to blue, to green and finally to a brownish color upon sol-precipitation. This solution was aged for 16 h in pure oxygen bubbling at 50 ml min⁻¹. After aging, the solution was allowed to settle at room temperature for 24 h. Then the precipitant was centrifuged (3000 rpm) and washed in ethanol and water several times to remove the unreacted impurities. The final particles were dried overnight at 60 °C and heated for 2 h at 300 °C to remove the solvents. The obtained product was used for further characterization and electrode-making processes.²³ The schematic chemical reactions are described below in equations (2.1-2.2):

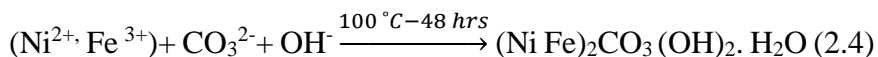


2.1.2.3 Preparation of NiFeO_x

The urea-assisted hydrothermal method was used to obtain the cylindrical shape nanoparticle in Paper 4¹¹⁹. The nickel and iron chloride salts and urea were dissolved together in 5:10:35 mM ratios in 80 ml distilled water. The solution was autoclaved (100 bar) in a Teflon-lined steel vessel at 100 °C for 48 h. The reacted product was centrifuged and washed several times in deionized water and

ethanol. The product was dried and sintered at different temperatures for 4 h (100, 250, 450 and 600 °C at the rate of 2 °C min⁻¹).

The corresponding reactions are given in the following equations (2.3-2.5):



2.1.3 Composite air electrode preparation

The composite electrode has an electrocatalyst layer, a current collector (Ni mesh), and a PTFE layer, which are sandwiched one over another in a series (Paper 2). The catalyst layer is prepared by mixing all ingredients with D-70® Shellsol at a required ratio, as shown in Table 2.3, in a Waring® laboratory blender (LB20ES) at 6000 rpm. The mixed solution was filtered and the retained paste was rolled onto a 100 mesh Ni-screen. The pasted electrode was mechanically pressed at 375 kg cm⁻². After this, another side of the electrode was brush painted by 20 wt.% PTFE solution. The roll-compacted electrode was sintered at 325 °C in N₂ atmosphere. The final electrode dimension was 30*50*0.35(±0.05) mm,³ and the active materials loadings are shown in Table 2. 3.

Table 2.3 Electrode compositions for the gas diffusion electrodes used for ORR/OER

Materials	Materials wt. %	Mass loading (mg cm ⁻²)	
		Based on LCMO	Based on Co ₃ O ₄
LCMO/ Gr/ PTFE	70/15/15	34.2	–
Co ₃ O ₄ / Gr/ PTFE	70/15/15	–	32.3
LCMO/ Gr/ Co ₃ O ₄ / PTFE	55/10/20/15	23.2	8.2
20% Pt/Vulcan XC-72/ PTFE	80/20	6.5	–

Gr=graphite; LCMO= La_{0.1}Ca_{0.9}MnO₃

2.1.4 Physical characterization

2.1.4.1 XRD

The X-ray diffraction of the synthesized samples and used electrodes was performed in the Siemens Bruker D5000 Diffractometer. The Cu K α radiation source ($\lambda=0.154$ nm) with 40 kV and 30 mA was used in a 2θ range of 10–70 ° at a speed of 0.02° per 12 s. The phase identification was done in Eva software (version 13.0.0.2007) with the PDF-2 (Powder diffraction file) database.

2.1.4.2 N₂ physisorption

Surface area and pore volume analysis was performed in Micromeritics ASAP 2010 at liquid nitrogen temperature (-196 °C). The Brunauer-Emmett-Teller (BET) method was used to calculate the surface area. Pore size and volume were measured using the Barrett-Joyner-Halenda (BJH) method.

2.1.4.3 Scanning and transmission electron microscopy (SEM-TEM)

The surface morphology and Energy-dispersive X-ray spectroscopy (EDX) of the samples was performed using the Zeiss Ultra-55 scanning electron microscope (SEM). The samples were used as synthesized or dried electrodes. The high-resolution transmission electron microscope (TEM) images were obtained from JEOL JEM-2100F.

2.1.4.4 X-ray photoelectron spectroscopy (XPS)

The oxidation state of the samples was analyzed using PHI Quantum 2000 scanning XPS microprobe with monochromatic Al K α radiation. The spot size and energy resolution were set to be 0.1 \times 0.1 μm^2 and 0.3 eV. The intensity of the peak was calculated from the area above the background to fit-XPS software.

2.1.4.5 Raman spectroscopy

The Raman spectrum was measured using an imaging spectrometer (iHR550, Horiba Jobin Yvon) in confocal geometry, using the light excitation of 532 nm. Further, the scattered light was filtered around 532 nm using a notch filter at $\pm 50 \text{ cm}^{-1}$.

2.1.5 Electrochemical measurements

2.1.5.1 Iron electrode testing

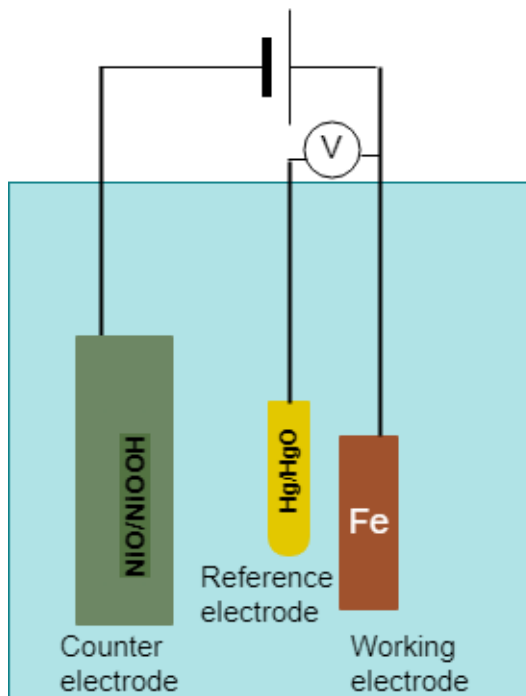


Figure 2.1 Schematic diagram of the testing cell with three-electrode setup;

The three electrodes set up were used in iron electrode studies, as shown in Figure 2.1. The iron composite electrode as a working, a conventional sintered nickel electrode ($\text{Ni}(\text{OH})_2/\text{NiOOH}$) as a counter electrode, and Hg/HgO was used as a reference electrode. The experiment was conducted in 6 M KOH solution, while in the Li experiment, 6 M KOH+0.65 M LiOH was used as the electrolyte.

The galvanostatic cycling (charge-discharge capacity test) and rate capability test of the electrodes were studied on the Land battery testing system (CT 2001–5 V 2A BTS System). The electrodes were

charged and discharged at 200 mA g^{-1} and 100 mA g^{-1} (approx. C/5 and C/10 h).

The cyclic voltammetry (CV) and polarization experiments were performed at 1 and 0.167 mV s^{-1} , respectively, on SP-50 potentiostat (Biologic Science Instruments).

For the galvanostatic polarization, step current was varied from 1 mA cm^{-2} to 15 mA cm^{-2} and the step duration was 5 minutes. The reported results were mass transfer and ohmic resistance corrected¹²⁰.

The impedance measurement was conducted on a fully charged electrode from 100mHz to 100kHz with 5 mV AC amplitude on Gamry PCI 4 G750 potentiostat, while the analysis was performed on Biologic science instrument with software (EC-Lab 10.44).

In Paper 3, *in operando* charge efficiency measurements were conducted in a two-electrode setup with special provision to the sample of the evolved gasses in mass spectrometry. The cell setup and equipment description were based on Svengren et al.'s earlier work¹²¹. Here, a formed iron electrode (2.25 cm^2) was cycled against the sintered Ni electrode (9 cm^2). All the electrodes were subjected to three different charge current densities 5, 10 and 15 mA cm^{-2} and a discharge current density of 5 mA cm^{-2} for three cycles.

2.1.6 Air electrode testing

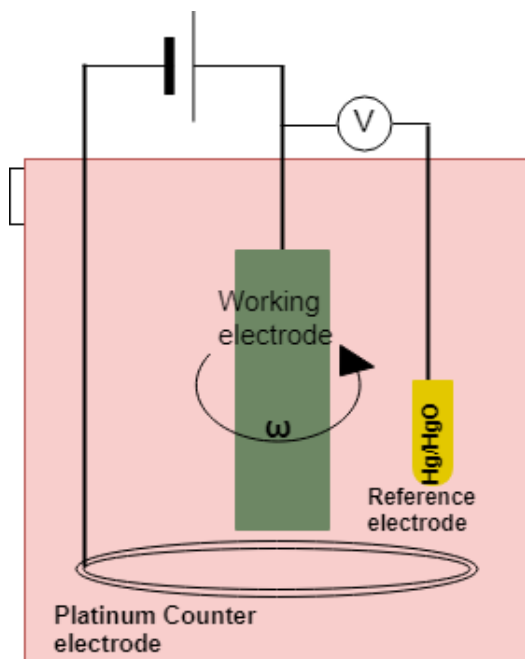


Figure 2.2 Schematic diagram of the RDE testing cell; Glassy carbon-working electrode, Hg/HgO-Referenced electrode and Pt counter electrode⁷¹

performed either in 1 M or 0.1 M KOH. The fresh RDE electrodes were also activated by running 15 cycles of CV scans in 0.1 to -0.9 V vs. Hg/HgO at N₂ saturation. Then the RDE experiment was performed in O₂ saturation in the range of 0.70 V to -0.90V vs. Hg/HgO. The RDE experiments were performed at a rotation speed of 500 to 2500 rpm. The Koutecky–Levich equation was employed to find the number of electrons (n) involved in the ORR ²³.

The bi-functional stabilities of the electrodes were conducted on gas diffusion electrodes. The catalyst side was exposed to 6 M KOH, while the PTFE side was kept dry and exposed to pure oxygen. The

stability test was conducted by 50 potential cycles: -0.35 to 0.70 V vs. Hg/HgO at 5 mV s⁻¹ scan rate. Meanwhile, the same test was done on NiFeO_x on glassy carbon substrate instead of gas diffusion electrodes.

Table 2.2.4. Electrode composition used on GC electrode in RDE experiment

Paper	Type of catalyst	Composition wt. %	Catalyst loading (mg cm ⁻²)	
			Based on LCMO	Based on Co ₃ O ₄
Paper 2	LCMO/ Gr/Nafion	75/20/5	0.47	-
	Co ₃ O ₄ / Gr/Nafion	75/20/5	-	0.47
	LCMO/ Gr/ Co ₃ O ₄ / Nafion	60/13.3/22.2/5.4	0.44	0.15
	20 wt.% Pt on Vulcan/ Nafion	91.3/8.7	0.09	-
Paper 4	NiFeO _x / Gr/Nafion	70/15/15	0.125, 0.25 and 0.75 mg cm ⁻²	

Gr=graphite (Timrex HSAG 300, Timcal Ltd); LCMO= La_{0.1} Ca_{0.9} MnO₃

PART III: RESULTS AND DISCUSSION

PART III RESULTS AND DISCUSSION

3 Results and Discussion

This chapter summarizes the important results attached to this thesis. The results of the iron electrode materials testing are presented and discussed in chapter 3. After that, the air electrode results are summarized and explained in chapter 4.

3 Studies on Cu and Sn-doped nano iron electrodes

This section summarizes the results from papers 1 and 3 appended to this thesis. The samples' details, characterization method, and procedure are elaborated in sections 2.1.1 and 2.3.

3.1 Phase identification of the Cu and Sn doped iron samples

Figure 3.1a and b present XRD patterns of Fe with Cu and CuSn (CuSn (a) and Sn (b) samples. All three samples have α -iron as a major phase. The Cu sample also has iron carbide (cementite and cohenite) and metallic copper as other minor phases and Scherrer crystallite size at iron plane reflection ($211-2\theta$: $44.5-45^\circ$) is about 52 nm. Fe_3SnC was also observed as a minor phase in only the Sn sample; when 2 wt.% Cu was introduced with 2 wt.% Sn, with traces of Fe_3SnC . There were no metallic phases of Cu, Sn and carbon phases due to the low concentrations of the respective elements. Though the TGA and EDX measurement showed more than 20 wt.% carbon, it was not observed in XRD, which suggests that carbon is in the amorphous phase. This carbon may improve electrode conductivity, as a porous network contributes to ionic conductivity^{122, 123}. Also, carbon might buffer the volume expansion and improve electrical conductivity along with Cu, and Sn of the iron electrode during the electrochemical cycling¹²⁴.

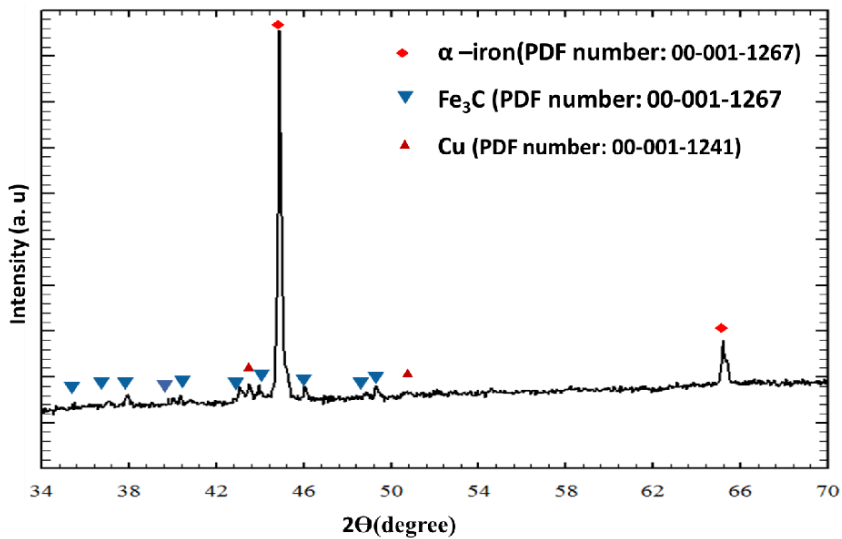


Figure 3.1a Powder XRD pattern of the 2 wt.% Cu- Fe-C

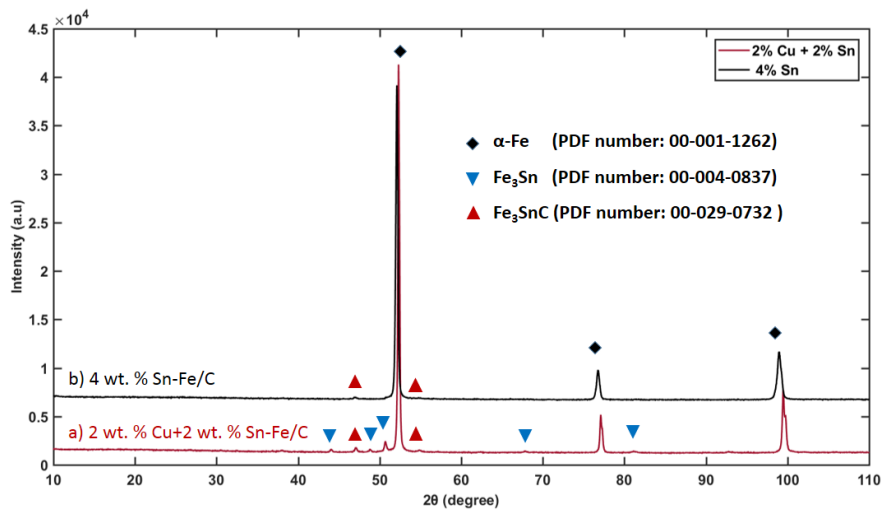


Figure 3.1b. XRD patterns of the a) CuSn and b) Sn doped iron samples

3.2 Surface and porosity of Cu and Sn doped iron samples

The BET surface area analysis was performed to find details about surface, pore size distribution, and isotherm type, which are shown in Figure 3.2 and Table 3.1. The Cu-doped sample showed low surface area and pore volume. The main difference between the Cu and the other samples was the carbon content. The Cu-doped sample had 10 wt.% carbon in iron carbide form, while the other samples had 21 to 24 wt.% carbon. The Cu sample had type IV isotherm with H3 hysteresis loop, and uniform pore size distribution. The other Sn and CuSn isotherms had a complicated pore structure with more microporous structure; for the Sn sample, the isotherm was similar to a Type II, H2, and H4 hysteresis loops, which was the result of complex interconnected and slit-shaped pores, which are formed by aggregates and agglomerates of platelet-sized particles that have slit-shaped pores of a microporous/mesoporous structure. The CuSn had a similar isotherm, but the hysteresis loop differed as a result of contributions from uniform micropores, as well as the presence of interconnected ink-bottle-shaped pores. In the TEM analysis, only Sn doping resulted in a wide particle size and shape, while in the Cu-doped sample, particle size was uniform.

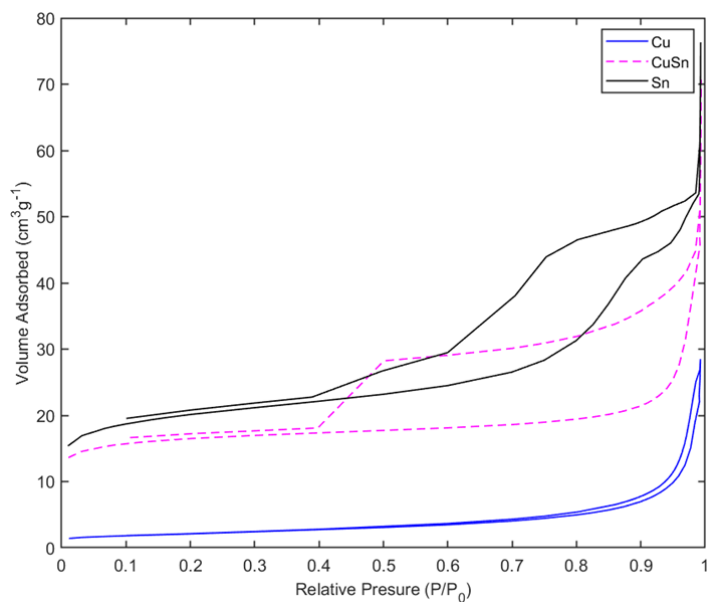


Figure 3.2. The N_2 isotherm of Cu, CuSn, and Sn-doped iron materials.

Table 3.1. BET surface areas and pore characteristics.

Sample	BET surface area($m^2 g^{-1}$)	Pore volume ($cm^3 g^{-1}$)	Average pore size (nm)
Cu	7.4	0.04	22.7
CuSn	55.0	0.09	8.0
Sn	69.2	0.11	9.6

3.3 Morphology of the Cu and Sn doped iron samples

Figure 3.3(a–c) shows TEM and selected area electron diffraction (SAED) image of Cu sample. In Figure 3.3 (a–b), the particles were present in a core-shell structure with sizes varying from 20 to 100 nm. Also, one to four particles showed agglomerate iron into one bigger particle. The shell thickness was around 20 nm, as shown in Figure 3.3c. The inset Figure 3.3c shows the SAED pattern of core and shell. The core diffraction interplanar distance was 1.04 Å, while the shell's interplanar distance (1.82 Å) was different from the core. This interplanar distance corresponded to α -iron (220) plane and Fe₃C (cohenite) (122) plane, respectively. This shell carbide layer might help to prevent nanoparticle growth and agglomeration. The TEM-SAED results also endorsed the XRD findings as α -iron and Fe₃C cohenite¹²⁵.

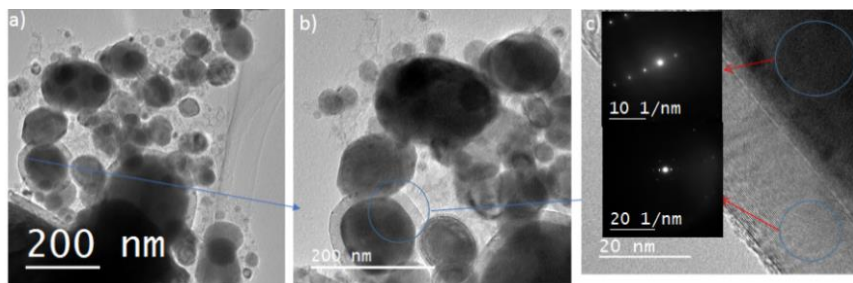


Figure 3.3. TEM image of Cu sample; a) TEM b) HRTEM; c) SAED pattern

TEM images of CuSn and Sn samples are shown in Figure 3.4. Figure 3.4a shows the particle morphology of the CuSn sample, which had particle sizes varying from 100 to 300 nm spread over the thin sheet of the carbon layer. The Sn sample (Figure 3.4b) had an uneven and irregular particle size (30–150 nm). Overall, based on TEM mass contrast, the CuSn sample had a dark and interconnected particle, while the Sn sample consisted of thinner and lighter platelet-shaped particles. Therefore, closely sintered and interconnected CuSn particles might have higher electrode conductivity and enhance electrochemical performance¹²⁶.

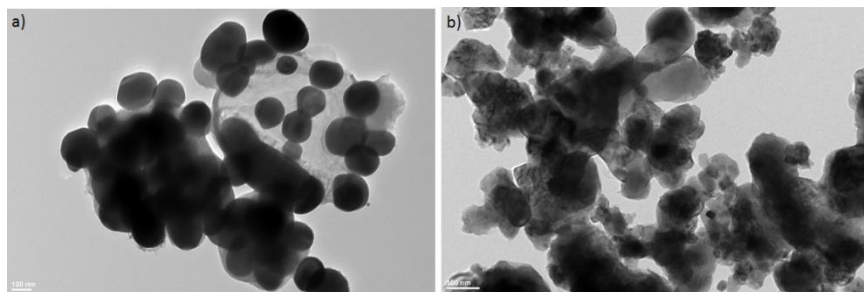


Figure 3.4. TEM images of CuSn (a) and Sn (b)

The XRD, and TEM showed the presence of metallic iron, iron carbide, and iron alloys with Cu and Sn. In the Cu sample XRD and TEM-SAED results confirm all major constituents completely, while in the CuSn and Sn samples a higher presence of carbon (24 wt.%) did not illustrate any major phase in the XRD. TEM was not even helpful to detect the lattice space or SAED. In this situation, we decided to check the CuSn sample in XPS and Raman spectra for more details about the metallic and carbon species.

3.4 Analysis of surface oxidation state and species of Cu doped iron sample

Figure 3.5(a–e) shows the XPS analysis of the CuSn sample. The Fe2p spectrum is shown in Figure 3.5a. Here, iron's metallic and 2+ oxidation species, which are characteristic peaks, were detected at 706.7 eV, 711 eV and 724.5 eV. The Cu2p spectrum is displayed in Figure 3.7b. The peaks for Cu(0), Cu(I) and Cu(II) were observed at 932.6 and 933.6 eV, respectively. The Sn3d_{5/2} spectrum (Figure 3.5c) showed two peaks: one at 486.9 and another weak shoulder peak at 485 eV, related to SnO or SnO₂ and metallic Sn, respectively. The O1s spectrum (Figure 3.5d) showed two characteristic peaks: one at ca 530 eV related to iron and tin oxides and the second peak at 532.6 eV related to hydroxyl species¹²⁷. Figure 3.5e shows the presence of carbon in the sample as a sharp peak at 284.8 eV. The XPS results confirmed the presence of copper, iron, and tin species in metallic or oxide form on the surface.

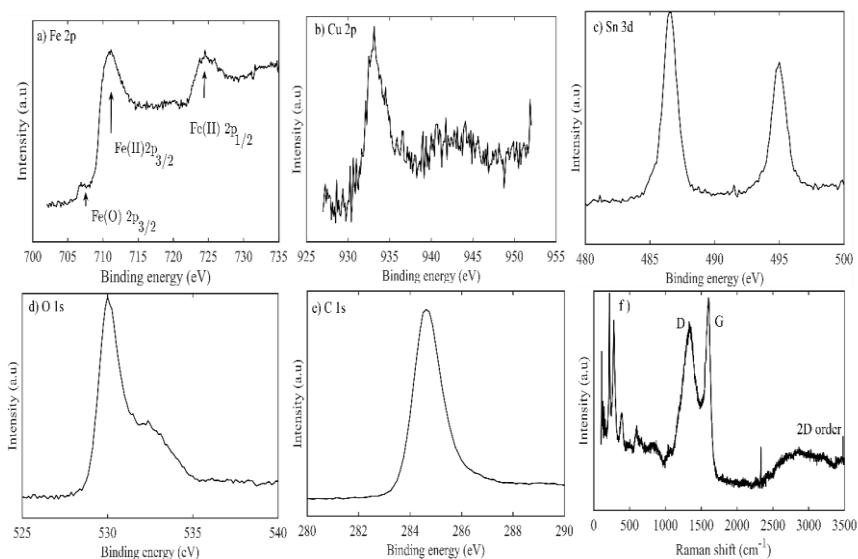


Figure 3.5. (a–e). XPS analysis of CuSn (f) Raman spectrum for the CuSn sample

To know more about the carbon species in the CuSn sample, Raman analysis was carried out (Figure 3.5f). The prominent peaks observed at 216, 277, 401 cm⁻¹ were for Fe₂O₃¹²⁸, and other peaks were at 1340, 1607 cm⁻¹ for characteristic carbon D and G band peaks. Besides, there was a weak diffuse peak at 2700 cm⁻¹ for the 2D band. The D band was not observed in defect-free Highly Ordered Pyrolytic Graphite (HOPG), but became Raman active due to defects within the graphene planes¹²⁹. The D and G band ratios give information about the degree of graphitization. I_D/I_G value was 0.64. The weak D band and the (I_D/I_G) might suggest the sample was conductive and partially graphitized¹³⁰. This could confirm that the carbon in the sample was amorphous. Also, the FeO_x peak demonstrated that the particles were not coated by carbon or carbide, as in the Cu.

3.5 Electroanalytical Characterization of Cu and Sn doped iron sample

3.5.1 Cyclic voltammetry of Cu doped iron

The electrochemical redox activity of the Cu-doped iron was examined using cyclic voltammetry. Figure 3.6 shows cyclic voltammogram from first to tenth cycles. During an anodic sweep of initial cycles, a broad peak was observed (-1 V to -0.7 V) consisting of two shoulders at -0.825 V and -0.76 V, corresponding to Equations 3.1 and 3.5, respectively, where the hydroxide ion chemically reacts to form the in situ sulfide formation at the electrode structure^{28, 131}. This formation is entirely dependent on the availability of iron (II) hydroxide. This double peak evolved to be a single peak from five cycles onwards. At cycle ten, three well-developed anodic peaks were observed at A₀ (-0.966 V), A₁ (-0.70 V), and A₂ (-0.44 V). The peak A₀ was related to the adsorption of hydroxide ion (Equation 1)¹³², where the A₁ peak was related to oxidation of Fe to Fe(II) (Equation 2), and A₂ related Fe(II) to Fe(III) formation (Equation 3). The redox reactions are shown in equations 3.1 to 3.5^{28, 132, 133}.

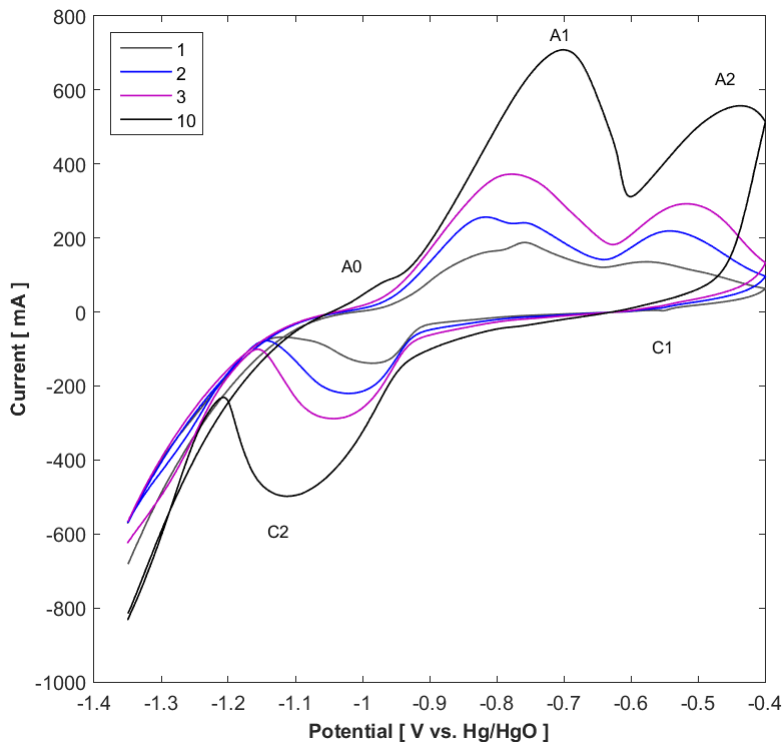
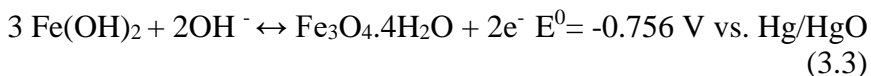


Figure 3.6. Voltammogram of Cu.



The A₀ peak position changed according to the nature of the electrode material^{46 47 134}. Apart from peaks A₀, A₁, and A₂, there was no other peak for Cu or iron carbide, as these were present in XRD and electron diffraction. The copper oxidation was not visible, due to its relatively low amount, and because it may have been masked by a parallel reaction (Fe(II)/Fe(III)). In all our experiments,

electrodes were only cycled between the iron oxidation up to a 2+ oxidation state (-1.2 V to -0.75 V vs. Hg/HgO). Therefore, in our potential operating range, the Cu and iron carbide were stable enough to maintain their desired function. The reduction direction had two peaks: one at C_1 at -0.55 V for the redox reaction of $\text{Fe}(\text{OH})_2/\text{FeOOH}$, which faded after two cycles⁴⁷. The second broad peak (C_2) occurred at -1.12 V for $\text{Fe}(\text{OH})_2/\text{Fe}$, and shifted cathodically when the number of cycles increased. The broad C_1 peak is for the reduction of several species (Fe_3O_4 to $\text{Fe}(\text{OH})_2$, $\text{Fe}(\text{OH})_2$ to Fe). Following this, hydrogen evolution was predominant from -1.21 V. The Cu-doped iron exhibited a very high reduction current (0.5 A) at a peak potential of -1.12 V, which is favorable for better utilization and battery operations at high discharge rates.

3.5.2 Cyclic voltammetry of Cu, CuSn and Sn doped iron

Figure 3.7 shows the CV response of the Cu, CuSn, and Sn-doped iron materials in the electrode operation potential window. As described earlier, in anodic sweep first hydroxide adsorption, and subsequent electrochemical oxidation of iron-to-iron hydroxide peak were observed. While on the reduction direction hydroxide and hydrogen evolution peaks were found. For the anodic direction, Sn-doped iron had higher oxidation currents, while in the Cu-doped iron, the oxidation current was lower, but the reduction happened with lower cathodic potential (-1.1 V), which is beneficial in terms of yielding better charge utilization. Therefore, the Sn substitution increased the anodic current, and Cu reduced the iron reduction potential.

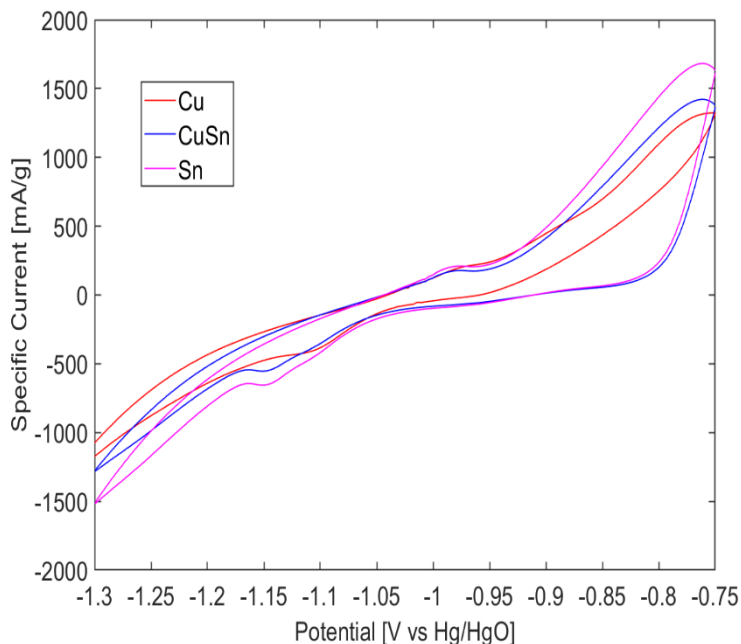


Figure 3.7. Voltammogram of Cu, CuSn, and Sn-doped iron.

3.5.3 Electrode kinetics

Figure 3.8 illustrates the passivation characteristics of Cu-doped iron. Potentiodynamic polarization was used to study passivation, which is a phenomenon where anodic oxidation is limited by a hydroxide or oxide film. The electrode was polarized anodically towards the -0.75 V vs Hg/HgO. Current-limiting passivation was not observed in our electrode. Moreover, high current density (40 mA cm^{-2}) was achieved at -0.75 V. Therefore, our electrode can withstand a higher current discharge without passivation. This was due to the nanostructure of Cu doped iron with Fe_3C , in the presence of an admixture of bismuth sulfide, which improved the overall performance and conductivity of the electrode^{28,58}.

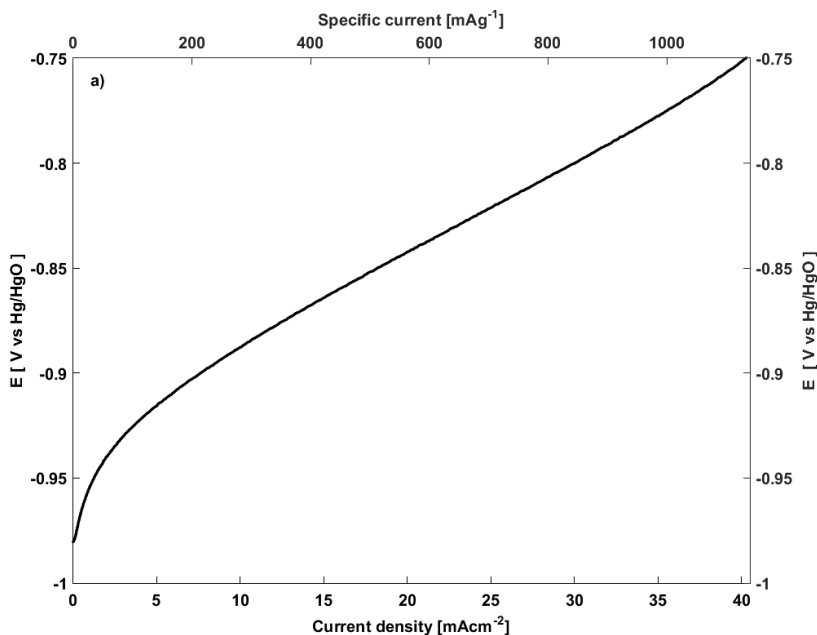


Figure 3.8. Potentiodynamic polarization of Cu-doped iron.

Figure 3.9 illustrates the anodic Tafel plot of a Cu-doped iron electrode, which was performed using the galvanostatic polarization method. The Tafel plot provided important kinetic parameters, i.e. Tafel slope and the exchange current density (i_0). These values were calculated in the low current regions; which were found to be 35 mV dec^{-1} with an exchange current density of $2.6 \cdot 10^{-4} \text{ A cm}^{-2}$. This slope provided information about the reaction mechanism and intermediate product surface coverage. Exchange current density depends on the type of materials used in the redox reaction, which provides information about reversibility in the anodic/cathodic direction. The Tafel slope for iron material with sulfur additives was $40 \text{ mV to } 80 \text{ mV decade}^{-1}$ ^{135,120}, and recently-reported carbon grafted active material had $30 \text{ mV to } 32 \text{ mV decade}^{-1}$ ³⁶. Our experimental slope value was low compared to reported data in the literature, which is close to $3RT/2F$. Based on the Tafel slope, reacting species' surface coverage ($\Theta=1$) is uniform, and changes according to potential. These values support that the Cu-doped iron

with an iron carbide shell most likely accelerated the electrode kinetics, with an efficient electron transfer reaction between the electrode/electrolyte interphase, which augmented the high current charge/discharge, with low overpotentials for the reaction.

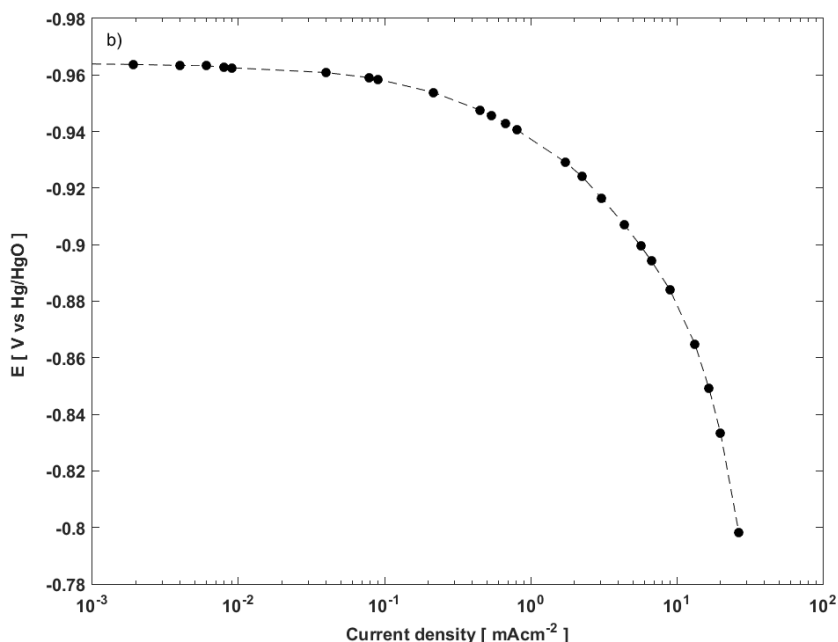


Figure 3.9. Galvanostatic polarization of Cu-doped iron.

The above CV and polarization results both directly and indirectly confirm that these Cu, CuSn, and Sn-doped samples are expected to perform well in battery electrode cycling.

3.6 Galvanostatic cycling of Cu, CuSn, and Sn-doped iron electrodes

3.6.1 Cu-doped iron electrodes cycling performance

Galvanostatic cycling of Cu-doped iron electrodes is shown in Figure 3.10 (a-b). The electrode composition is provided in the experimental part, Table 2.1.

Figure 3.10a) shows 300 cycles of charge-discharge profile evolution. In the initial cycles, the charging voltage was roughly -1.12 V, while after 300 cycles, the profile changed to -1.22 V. Additionally, the potential profile had two distinct plateaus, confirming the increased hydrogen evolution in later cycles. On the discharging plateau, initially, the cycle plateau was -0.95 V, then shifted into -0.90 V. This shift suggests increased ohmic resistance of the electrode, due to resistive products plugging the pore, thereby blocking access to the inner iron active sites ¹³⁶. Figure 3.10 b) shows the discharge capacity vs. cycle number. Up to 100 cycles, the specific capacity and efficiency were roughly 350 mAh g⁻¹ and 80%, respectively. After 100 cycles, the capacity waned gradually to 250 mAh g⁻¹, at 55% efficiency. This gradual decrease was related to sulfur disappearance from the iron electrode, and to the electrodeposition on the Ni counter electrode. The remaining iron electrode without sulfur left the electrode by increasing the resistance, and thereby increased hydrogen evolution ²⁸.

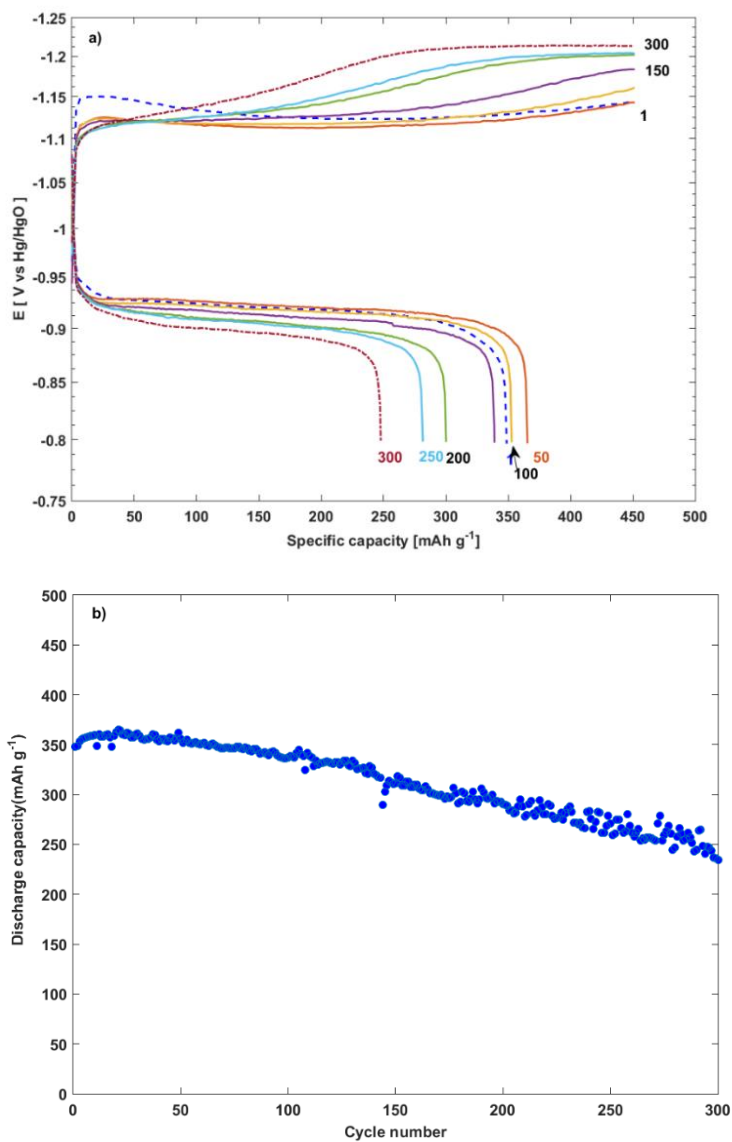


Figure 3.10 (a-b) Galvanostatic cycling profile and specific discharge capacity of electrode vs cycle numbers of Cu-doped iron electrode.

Figure 3.11 shows the Cu-doped iron's rate capability performance: a) discharge profile at different specific currents; b) discharge capacity vs cycle number. Figure 3.13a shows the specific current as 50 mA g^{-1} to 500 mA g^{-1} , while electrode discharge capacity was kept constant at roughly 350 mAh g^{-1} to 358 mAh g^{-1} , with 80% current efficiency. The only change observed was that the discharge voltage profile shifted from -0.95 V to -0.875 V . The discharge rate of 900 mA g^{-1} (32 mA cm^{-2}) saw a capacity drop to 48 mAh g^{-1} , which is closer to the mass transport limited region (-0.8 V - 30 mA cm^{-2}), as shown in the Tafel plot (Figure 3.9). At 900 mA g^{-1} , the electrode passivation limited the hydroxyl ion in terms of reaching the iron site within the internal pores. Following the high current discharge, the electrode was able to bounce to its original capacity at lower discharge currents, as shown in Figure 3.11b.

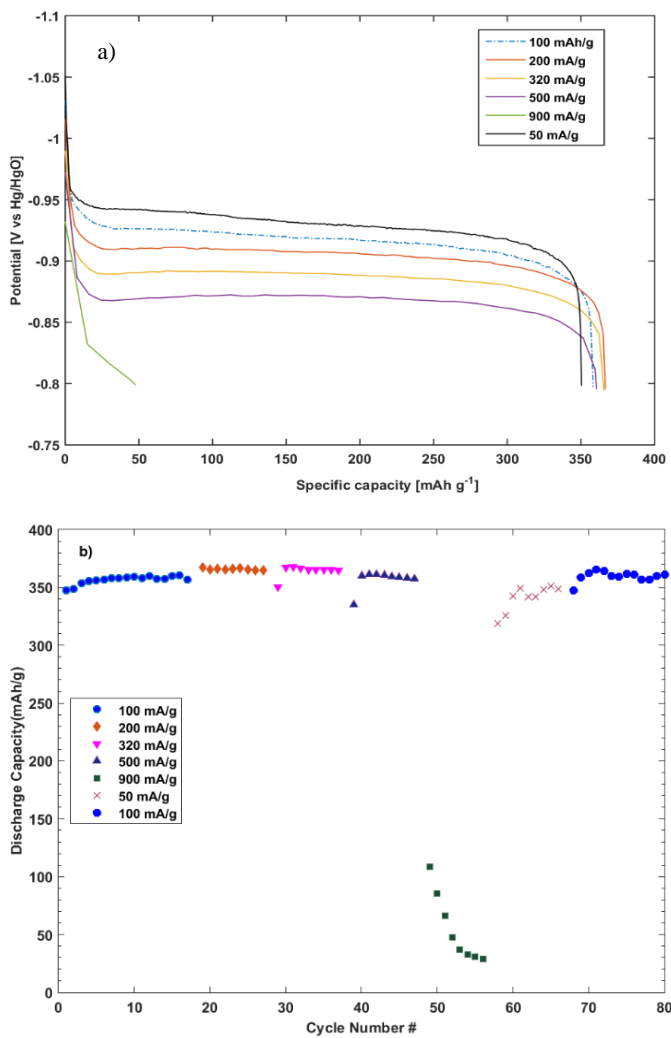


Figure 3.11. Rate capability of Cu-doped iron; a) discharge profile of electrode at different current rates; b) discharge capacity at different rates vs cycle number.

3.6.2 CuSn and Sn-doped iron electrodes cycling performance

Figure 3.12 illustrates the charge-discharge profiles for the CuSn electrodes and Sn-doped iron electrodes. The electrode composition and loading details are provided in the experimental part 2.1. Here, plain electrode charging profiles indicated a higher negative potential, while the addition of LiOH and CNT decreased the overpotential for iron reduction from -1.15 V to -1.10 V vs. Hg/HgO. The initial electrochemical cycle performance is shown in Table 3.3. The CuSn-doped iron samples demonstrated the highest discharge capacity, more so than the Sn-doped sample (378 mAh g⁻¹-77%-charge efficiency). This indicates that 4 wt. % Sn is not beneficial to the CuSn sample for improving the electrode performance. The CNT addition increased the capacity from 434 mAh g⁻¹ to 470 mAh g⁻¹ at 90% efficiency.

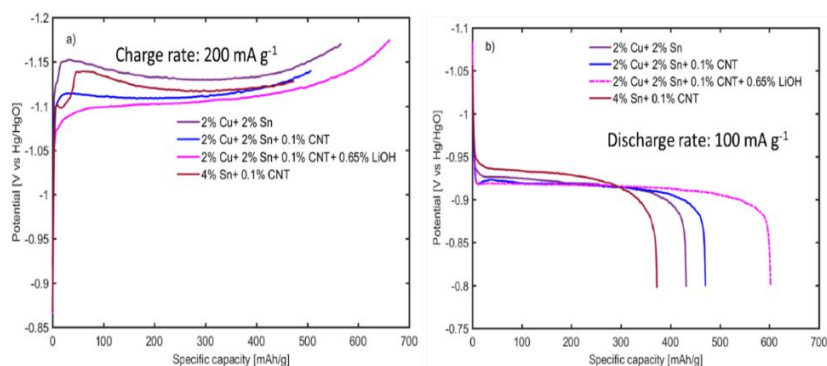


Figure 3.12. Galvanostatic charge-discharge profiles for CuSn and Sn-doped iron electrodes (a-b).

Adding additional LiOH to electrolytes increased discharge capacity further to 603 mAh g⁻¹. The increased discharge performance for the CuSn-doped iron sample occurred as a result of CNT addition, which also enhanced the conductivity arising from the Cu and semi-amorphous graphitic carbon network and uniform particle size, allowing the electronic and ionic transport in electrodes. As such, these factors support an ideal reaction site for a charge/discharge

reaction^{137, 138}. The LiOH altered iron dissolution significantly, and formed a porous hydroxide which enhanced the electrolyte access to the active material⁴³.

Table 3.2 Initial cycles charge/discharge performance for Cu and Sn-doped iron electrodes.

Electrode	Discharge capacity (mAh g⁻¹)	Charge efficiency (%)
CuSn	434	82.6
CuSnCNT	470	93
CuSnCNTLi	603	91.3
SnCNT	378	76.7

The cycle life of CuSn and Sn-doped iron electrodes are shown in Figure 3.13. The highest capacity for the CuSnCNTLi electrode reached 50% from 600 mAh g⁻¹ (at first cycle), to 300 mAh g⁻¹ at the 225th cycle, at a loss of 1.3 mAh g⁻¹/cycle. Concurrently, the CuSnCNT electrode, up to 450 cycles, was the last to reach the 50% charge efficiency at a capacity of 277 mAh g⁻¹, from 470 mAh g⁻¹ at first cycle, at a loss of 0.41 mAh g⁻¹/cycle. The added LiOH electrode had poor long-term stability. The reason for this was the poor mechanical stability of the electrode, which worsened due to the high porosity, resulting in active material loss from the electrode⁴³. The SnCNT sample exhibited a less stable performance, reaching the 50% charge efficiency mark in 120 cycles; its capacity loss was even higher than the other electrodes, at a loss of 0.96 mAh g⁻¹/cycle.

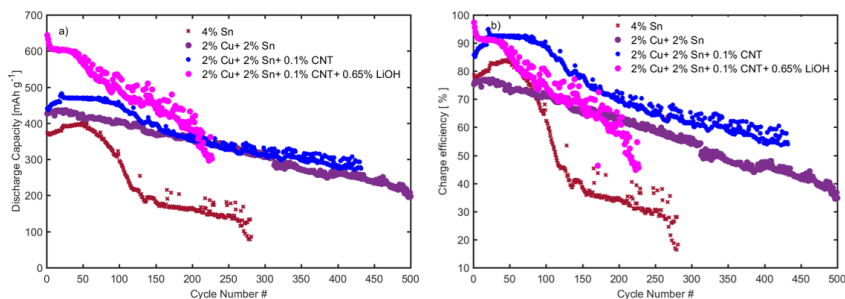


Figure 3.13. Discharge performance of Cu and Sn-doped iron electrodes at different rates vs cycle number.

In our previous studies, Cu-doped iron achieved a stable discharge capacity of 367 mAh g^{-1} with 80% charge efficiency¹³⁹. When comparing the three materials – Cu, CuSn, and Sn-doped iron electrodes – the Sn-doped sample showed poor performance in terms of capacity and life cycle. The reason for this may be because of Sn's low conductivity and high overpotential during reduction of iron (Figure 3.7 in CV image), and its non-uniform particle size distribution, as in TEM 3.3b.

The doping of Sn on Cu increased the discharge capacity. Additionally, using different additives such as LiOH and CNT may also have increased electrochemical performance, by altering conductivity and porosity. Concurrently, the higher porosity also increased interparticle resistance, compared to metallic conductors. The cycling caused interparticle resistance to increase. The disappearance of the active material from the electrodes, increases capacity decay by reducing the charge acceptance of the iron reduction.

3.6.3 Effect of charge current density on hydrogen evolution and electrode performance on Cu, CuSn, and Sn-doped iron electrodes

In situ charge efficiency measurements were performed using GC mass spectrometry, coupled with electrochemical cycling. The experimental setup, amount of evolved hydrogen, and

corresponding coulomb calculation method were adopted from Svengren et al ¹²¹. We studied the effect of current densities (5, 10, and 15 mA cm⁻²) on charge acceptance, as well as discharge performance on the CuSn and Sn electrodes.

The results are shown in Figure 3.14(a-d). The top plot in each sample shows the relationship between cell potential and hydrogen generation velocity vs time. The bottom plot shows the charge efficiency and cumulative hydrogen capacity vs time. Hydrogen generation counting time was extended to measure all accumulated gases in the system. A summary of the results is shown in Table 3.3. The charge efficiencies resulted in the following order: CuSnCNT > CuSn > CuSnCNTLi > SnCNT.

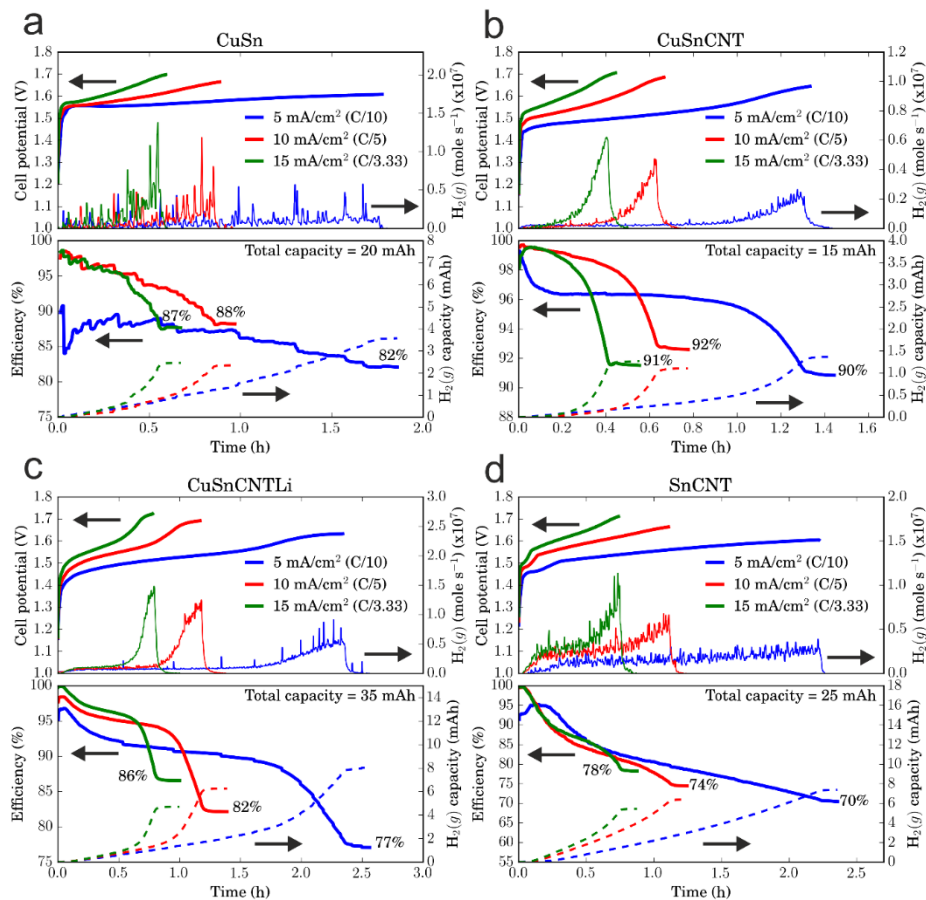


Figure 3.14. Charging efficiency measurements at 5, 10 and 15 mA cm⁻² of (a) CuSn; (b) CuSnCNT; (c) CuSnCNTLi; (d) SnCNT.

Table 3.3. Efficiency comparison of mass spectrometer vs potentiostat.

Sample	^aη_{charge} (5/10/15 mA cm⁻²)	^bη_{CE} (5/10/15 mA cm⁻²)
CuSn	82/88/87%	81/88/88%
CuSnCNT	90/92/91%	93/92/90%
CuSnCNTLi	77/82/86%	77/83/88%
SnCNT	70/74/78%	70/76/80%

a) $\eta_{\text{charge}} = \frac{Q_{\text{tot}} - Q_{\text{H}_2(g)}}{Q_{\text{tot}}}$ (note: charging efficiency is based on the difference between total and H₂(g) capacity).

b) $\eta_{\text{CE}} = \frac{Q_{\text{discharge}}}{Q_{\text{charge}}}$ (note: charging efficiency calculated using the VMP 3 Bio-logic potentiostat software).

CuSnCNTLi showed the lowest efficiency. By comparing all the charging plateaus, CuSnCNTLi indicated an extended hydrogen evolution plateau at potentials above 1.65 V, which is evident from Figure 3.14c. The efficiency evolution in the bottom image of Figure 3.14 indicates primarily three distinct slopes at the following potentials: 1) below 1.5 V; 2) between 1.5 V to 1.6 V; 3) above 1.6 V. In the below 1.5 V section, the amount of evolved H₂ was low, while the nucleation of Fe(OH)₂ to Fe took place. Following on, for the 1.5 V to 1.6 V part, a constant rate of H₂(g) occurred; here, both an iron reduction and hydrogen evolution took place. Finally, H₂(g) evolution was dominant above 1.6 V, via overcharging of iron electrodes. Overall, the highest charging efficiency was observed at high current densities. The optimum charge value was 10 mA cm⁻². Additionally, the samples containing Cu and CNT showed higher charge acceptance, due to enhanced conductivity. The charge efficiencies obtained through mass spectrometry and potentiostat obtained values were similar; only small deviations were detected, as shown in Table 3.3.

Based on coupled mass spectrometry and galvanostatic cycling of iron electrodes, in their charging profiles, electrodes with CNT showed distinct hydrogen evolution plateaus at 1.65 V vs. NiOOH, or -1.2 V vs. Hg/HgO. The continual higher rate of hydrogen evolution was not a favorable condition for the porous electrode structure, as it had the potential to destroy the electrode structure and the interconnectivity of particles. In CuSn, hydrogen evolution was not limited to a particular part, but extended along the entire charging plateau. The mass spectrometer data also confirmed this trend (Figure 3.14a). This shows that managing the hydrogen evolution rate can improve the mechanical stability and life-cycle of the electrode. One possible way of doing this is to apply a constant voltage charge, or through a combination of constant current and constant potential charging. Other important results include charging at a higher current density (10 and 15 mA cm⁻²), which improved charging efficiency, as shown in Table 3.3.

Among the electrodes tested, CuSn-doped nano iron samples' performance showed promise in terms of having high capacities and charge efficiencies, which varied from 434 mAh g⁻¹ to 603 mAh g⁻¹, and 81 to 93%, respectively, based on the additives (CNT, or CNT and LiOH). Our results were better than those reported in the literature^{46, 57, 139}.

3.7 Galvanostatic cycling effect on Cu-doped electrode

To study the cycling effect on electrodes, we monitored electrodes using EIS, XRD, and SEM for fresh, formed (35 cycles) and 200 cycles passed stage. These results are shown in the following section.

3.7.1 Impedance evolution along the galvanostatic cycling

EIS analysis was carried out on the Cu-doped electrode on fresh, formed and after 200 cycles. The corresponding Nyquist plot is shown in Figure 3.15. The impedance spectra was fitted to the model circuit shown in the inset, in Figure 3.15, using EC-Lab 10.44. The

results are shown in Table 3.4. The fresh electrode had high charge and ohmic resistance, as expected, due to hydrophobicity and lower porosity at the electrode/electrolyte interphase. The formed electrode indicated lower resistance (R_s , R_{ct}), due to activation changing the bulk conductivity, texture, and porosity of the electrode. The double layer capacitance value was proportional to the roughness and surface coverage of ions. Here, its value increased from that of fresh electrode to formed electrode, due to the uniform surface coverage of sulfur species ¹⁴⁰. Following 200 cycles, the electrode's ohmic resistance was surpassed, and the charge transfer increased significantly from the formed electrodes at 35 cycles. This suggests that the resistive component (uncharged passive iron hydroxide, sulfur depletion) occurred in the electrode/electrolyte interphase. Furthermore, the high value of the double layer capacitance arose due to the presence of iron oxides and increased surface roughness, as shown in Table 3.4. The electrodes' high surface area rendered a high capacitance of $320 \mu\text{F cm}^{-2}$, which is higher than the iron metals' capacitance value ($150 \mu\text{F cm}^{-2}$) in alkaline media ¹³⁶.

Table 3.4. Values of impedance measurements.

Resistance type	Fresh electrode	Formed electrode (35 cycles)	Cycled electrode (200 cycles)
Ohmic resistance, R_s (Ω)	0.2016	0.086	0.125
Charge transfer Resistance, R_{ct} (Ω)	0.050	0.04	0.08
Double layer Capacitance, ($\mu\text{F cm}^{-2}$)	320	380	4280
Roughness factor	25	33	1478

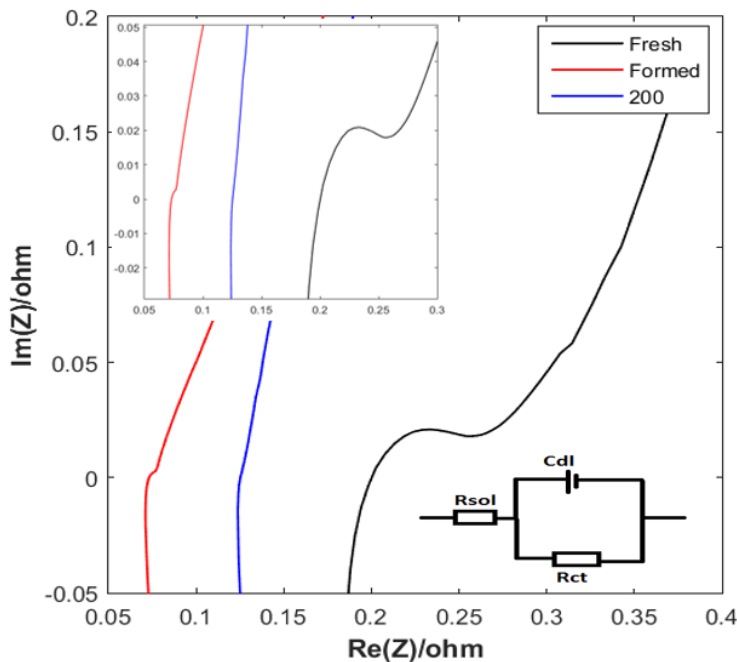


Figure 3.15. Impedance evolution of Cu-doped iron at different cycles

3.7.2 Ex-situ XRD phase evolution

The cycled electrodes phases were analyzed using X-ray diffraction (XRD on Cu-doped electrodes at fresh, formed (35 cycles), and 200 cycles, in both charged state.

Figure 3.16 a) shows the XRD phases of the charged electrode at different cycles. Four phases were observed in all patterns: α -iron, Fe_3C , Bi, $\text{Fe}(\text{OH})_2/\text{FeOOH}$. The iron hydroxide peak changed alongside the different cycles, due to the limited reconversion and growth of iron hydroxide. The crystallite size reduction and peak intensity suggest that the α -iron phase slightly decreased alongside the number of cycles, while iron carbide and iron (II) hydroxide peaks remained distinct. The crystallite size of the iron particles slightly decreased from the fresh electrode 52 nm to 200 cycles having 47 nm. The limited reconversion of discharged product and

sulfur disappearance lead to enriched iron hydroxide, reducing the overall performance of the electrode. However, the presence of iron carbide confirms that it maintained its core-shell morphology, without aggregation of the iron in the electrode structure.

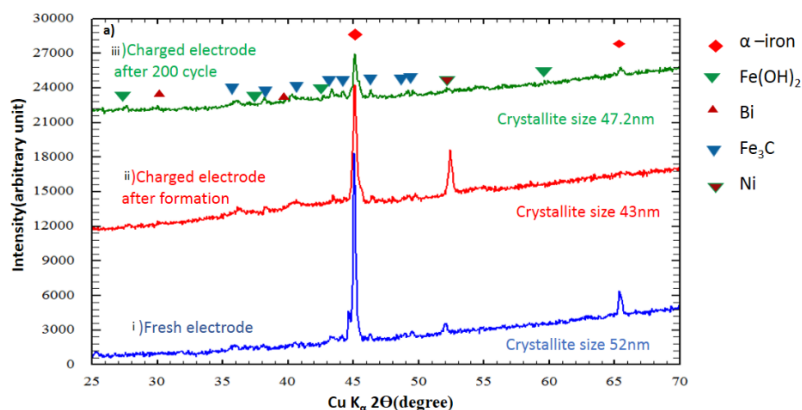


Figure 3.16. Ex-situ XRD evolution of cycled electrode; a) charged state electrode;

3.7.3 Ex-situ morphological evolution

Scanning electron micrograph (SEM) was used to analyze morphological changes alongside electrode cycling, as shown in Figure 3.17. Figure 3.17 (a and c) shows the morphology of the formed and 200-cycle electrodes at charged state; after 200 cycles, a decrease in particle size and an increased porosity occurred, similar to that observed in the XRD image in Figure 3.16. The discharged electrodes at formed and after 200-cycles are shown in Figure 3.17 (b and d), indicating the rough, whiskery and acicular-shaped particles of hydroxide crystals. Particle agglomeration or growth were not observed. These results corroborate that particle morphology remained constant throughout electrochemical cycling, due to the specific interconnectivity and core-shell type of iron and iron carbide.

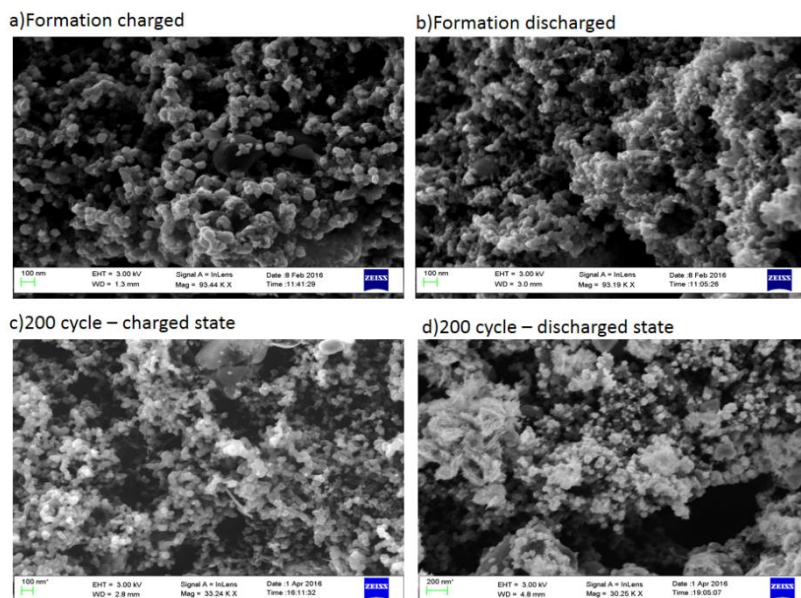


Figure 3.17. SEM of Cu-doped electrodes at different cycles (a and b after formation; c and d after 200 cycles).

TEM measurement was conducted on charged electrodes at the formed state, as shown in paper 1. The image confirms that the particles ranged between 20 nm and 200 nm, as in the initial powder material. The particles of iron and shell Fe_3C maintained their original core-shell nanostructure. As a result of the core-shell configuration, the nanostructure morphology was not changed after cycling. The XRD, CV, and TEM analyses confirmed that the iron carbide was not involved in the redox reaction at the potential operating range. As a result, the electrochemically active core and the inactive shell are favorable for retaining nanostructure stability against cycle-induced particle growth. Existing research indicates particle agglomeration as the main reason for capacity decay and poor performance in nanoparticles^{58, 133, 141}.

The current study highlights the outstanding charge and discharge performance of Cu and CuSn-doped iron electrodes. The typical high surface of nanoparticles favors particle agglomeration, which

was prohibited by an iron carbide layer or porous semi-graphitic carbon networks. Furthermore, Cu, CNT, and carbon are able to maintain constant electrode conductivity, irrespective of charge state ⁵⁹.

4 Electrochemical studies on mixed-oxide La-doped CaMnO_x and Co_3O_4 catalysts and NiFeO_x

In this part, the results from papers 2 and 4, appended to this thesis, are discussed. The samples synthesis and characterization method and the electrochemical testing procedures are discussed in sections 2.1.2 and 2.3.2.

4.1 Phase identification of synthesized particles

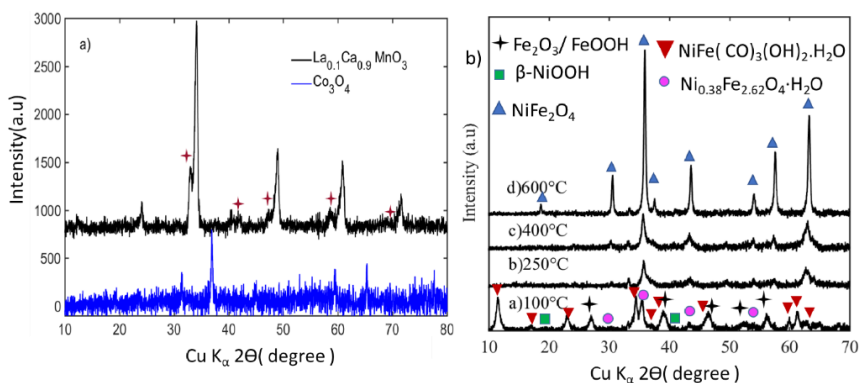


Figure 4.1 XRD patterns of a) $\text{La}_{0.1}\text{Ca}_{0.9}\text{MnO}_3$ and Co_3O_4 ; b) NiFeO_x the different annealing temperatures

Figure 4.1a shows the XRD patterns of $\text{La}_{0.1}\text{Ca}_{0.9}\text{MnO}_3$ (LCMO) and Co_3O_4 materials. The LCMO pattern belongs to the $\text{La}_{0.1}\text{Ca}_{0.9}\text{MnO}_3$ perovskite structure as a major phase, and also, peak splitting (marked $+$) was observed due to the substitution-induced crystal deformation, which produced the La MnO_3 structure, similarly observed in the $\text{La}_{1-x}\text{Ce}_x\text{MnO}_3$ ($x=0.2$) and oxygen deficient $\text{CaMnO}_{3-\delta}$ ($\delta=0.5$)^{142, 143}. There were no impurity phases, such as $\text{Mn}_2\text{O}_3/\text{Mn}_3\text{O}_4$, La_2O_3 , or CaO .

Co_3O_4 belongs to the face-centered cubic structure of the spinel type. The Scherrer average crystallite sizes were about 17 and 12 nm for $\text{La}_{0.1}\text{Ca}_{0.9}\text{MnO}_3$ and Co_3O_4 respectively, which were calculated

from the facets at (242) and (311) for LCMO and Co_3O_4 , respectively.

Figure 4.1b shows the XRD phase evolution of NiFe oxides at different calcination temperatures (100-600 °C). The initial starting sample (100 °C-pattern a) has three major phases: nickel iron hydroxide hydrate ($\text{Ni}_{0.38}\text{Fe}_{2.62}\text{O}_4 \cdot \text{H}_2\text{O}$), a layered double hydroxide carbonate phase ($\text{Ni}_{0.75}\text{Fe}_{0.25}(\text{CO}_3)_{0.125}(\text{OH})_2 \cdot 0.38 \text{H}_2\text{O}$), and an iron oxide hydrate phase ($\beta\text{-Fe}_2\text{O}_3 \cdot \text{H}_2\text{O}$). Moreover, two minor phases are NiOOH and FeOOH. At 250 °C (pattern b) calcination, the spinel nickel ferrite (NiFe_2O_4) was formed by the evaporation and decomposition of water and carbon dioxide from the LDH and hydroxide phases. Further calcination resulted in more crystallization of NiFe_2O_4 at 450 and 600 °C. The Scherrer crystallite sizes of the different samples are also confirmed by the particle size increase from 250 to 600 °C calcined samples, as shown in Table 4.1. Furthermore, heating increases the peak intensities at 35.9° and 65.3° 2θ , corresponding to (311) and (440) facets of NiFe_2O_4 . Therefore, calcination temperature affected the phases of the samples, crystallinity and crystallite size directly.

Table 4.1. Physical characteristics of all the samples

Sample	Crystallite size from XRD* (nm)	Specific area Φ ($\text{m}^2 \text{g}^{-1}$)	Mean pore diameter Φ (nm)	Pore volume Φ ($\text{cm}^3 \text{g}^{-1}$)
LCMO	17	21	6	0.035
Co_3O_4	12	64	27	0.44
NiFe 100 °C	13.85	131	23	0.81
NiFe 250 °C	10.59	127	25	0.82
NiFe 450 °C	13.53	118	15	0.51
NiFe 600 °C	26.66	40	56	0.41

* For the 100 °C sample, calculated at $2\theta - 11.5^\circ$; 250 to 600 °C calculated at $2\theta \approx 35.7^\circ$ Φ Calculated from N_2 adsorption-desorption curve

4.2 Surface area characterization

The surface area and porosity of LCMO, Co_3O_4 , and NiFeO_x are shown in Table 4.1. The hydrothermal synthesis yielded higher

surface ($60\text{--}130\text{ m}^2\text{ g}^{-1}$), while the co-precipitation method gave a moderate surface area. However, the heat treatment reduced the surface areas and pore volumes in the NiFe oxide samples. The high surface area of the materials permits the electrolyte to contact the catalyst, while the more open structure allows the transport, diffusion and adsorption of O_2 and hydroxide ions in the electrolyte

77.

4.3 Morphological characterization

Figures 4.2a) and b) show the surface morphology of the LCMO and Co_3O_4 . The TEM image of the LCMO (Figure 4.2a) shows that high-temperature sintering produced crystalline and well-connected particles. The particles are in rod and platelet-shaped thin sheets. This could reduce the charge transfer resistance in electrochemical reactions.

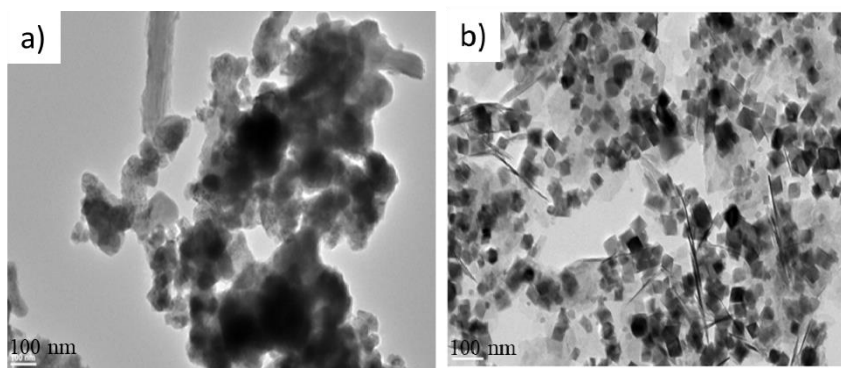


Figure 4.2. TEM micrographs of $\text{La}_{0.1}\text{Ca}_{0.9}\text{MnO}_3$ (a) and Co_3O_4 (b)

Figure 4.2b) shows a TEM image of Co_3O_4 . The particles are uniform, cubic-sized, and less than 30 nm, while some of the particles are in a platelet, nanoneedle-like morphology, less than 5 nm in diameter. The initial synthesis process produces the nanocrystals of $\text{Co}(\text{OH})_2$, which are being transformed into nanowires, according to Archer et al.⁹⁴. Longer reaction time, oxygen bubbling and stirring lead to oxidation of $\text{Co}(\text{OH})_2$ and further conversion to nanocubes, with less distinct nanowires. The

nanocubes of Co_3O_4 were prepared without templates, additives and thermal treatment.

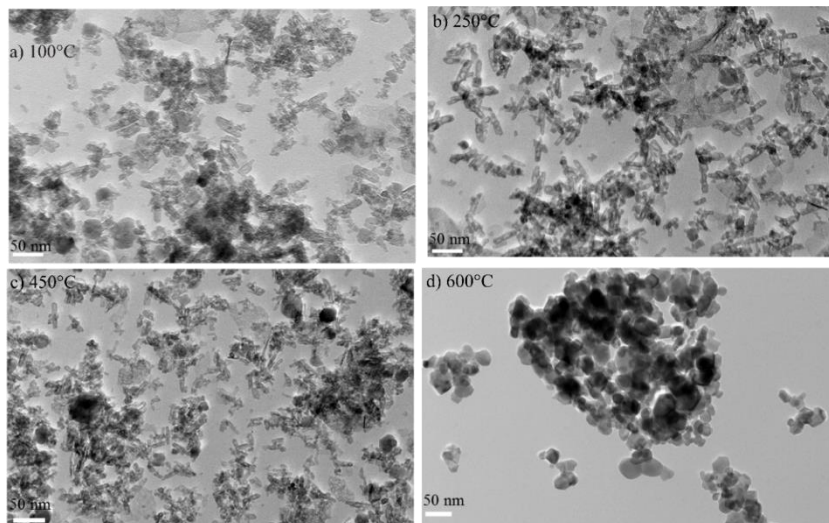


Figure 4.3. TEM image of Ni Fe oxide at the different temperatures

Figures 4.3(a-d) present TEM images of NiFe oxides. The samples calcined at 100-450 °C are mostly in nanorod, and a few, in thinly-elongated platelet morphology, as seen in Figures 4.3(a-c). However, starting from 250-450 °C, the particles started to agglomerate into bigger sizes and form cavities. At 600 °C, the particles changed into spherical and cubic structures, in accordance to the XRD results, in which the crystallite size dropped from 13.85 to 10.89 nm for 100 and 250 °C calcined samples. The particle size then grew to 13.53 nm at 450 °C, and finally, it reached 26.66 nm at 600 °C, as shown in Figure 4.3 and Table 4.1. Due to decarbonization and dehydration, the particle size reduced in the 250 °C sample, and also, due to the cavities as in the TEM image (Figure 4.3b). The TEM results confirmed that the particles are well-dispersed-nanorod structures, which are favorable catalytic-active sites for the oxygen redox reaction ¹⁴⁴.

4.4 Surface species characterization

The XPS spectra were recorded to analyze the surface oxidation state of the NiFeO_x samples. The XPS spectra of the survey spectrum, Ni2p, Fe2p, O1s, and C1s regions, are shown in Figures 4.5(a-d). The wide spectrum (Figure 4.5a) confirms the Ni, Fe, O and C species in the sample. At low-temperature calcination, O1s, Fe2p and Ni2p peaks were broad, with multiple features, while the temperature increase sharpens the peaks. This conforms with the XRD (Figure 4.2) as pure phases forming at higher temperatures. At low temperatures, Ni2p spectra showed the multiple peaks from 859 to 854 eV, corresponding to Ni 2+ to 3+ oxidation states. The presence of Ni(OH)_2 , $\text{NiFe(CO)}_3(\text{OH})_2$ gave multiple peak splitting due to the Ni ion being in different coordinations (octahedral and tetrahedral). The $\text{Fe2p}_{3/2}$ spectra of the four samples did not show any significant change. At 100 °C, the spectra look closer to Fe_2O_3 ^{145, 146} (around 712 eV) and $\text{NiFe(CO)}_3(\text{OH})_2$ (724 eV). Beginning at 250 to 600 °C, Fe2p spectra shifted to a lower (712 to 710 eV) in binding the energy of Fe in NiFe_2O_4 , and the spectra look closer to the NiFe_2O_4 ¹⁴⁷. O1s spectra also follow similar trends to the Ni spectra. At low temperatures, metal oxides, hydroxide and water peaks were detected¹⁴⁵ (Figure 4.5d). Further heating at 400-650 °C resulted as the only peak of metal oxide (NiFe_2O_4). The XPS results show multiple surface oxidation species of Ni, Fe and O at low temperature, particularly at 250 °C. Thus, XPS showed a wide range of surface functional groups.

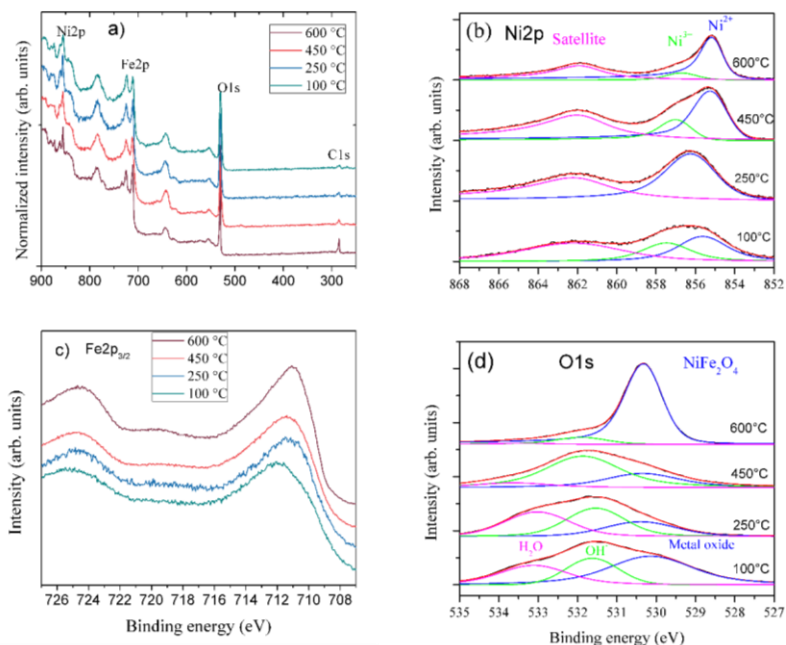


Figure 4.5. XPS characterization of a) whole range; b) Ni 2p; c) Fe 2p and d) O1s energy region from 100-600 °C calcined samples.

4.5 Electrochemical identification of redox activity

4.5.1 Cyclic voltammetry

The redox activity of the LCMO and Co_3O_4 samples was examined using cyclic voltammetry in N_2 saturated 1M KOH solution. The electrode composition is provided in section 2.1.2.3 and Table 2.3. Figure 4.6a) presents the CV response of LCMO/graphite/Nafion on the GC substrate. The anodic scan had two oxidation peaks: one big oxidation wave at 0.04 V corresponding to $\text{Mn}^{+3} \rightarrow \text{Mn}^{+4}$ and another small peak at -0.24 V vs. Hg/HgO, which is related to $\text{Mn}^{+2.67} \rightarrow \text{Mn}^{+3}$ reactions. After Mn^{+3} oxidation, oxygen evolution followed from 0.45, while, in the reduction direction, one single peak was observed at -0.16 V, which was assigned to the $\text{Mn}^{4+}/\text{Mn}^{3+}$ reduction. There was no further reduction of Mn to lower oxidation state. Therefore, LCMO perovskite showed only $\text{Mn}^{3+}/\text{Mn}^{4+}$ redox activity within its structure.

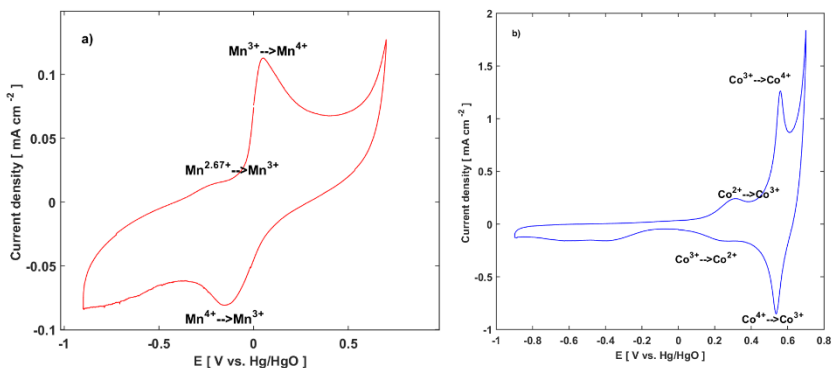


Figure 4.6a) LCMO and b) Co₃O₄ voltammogram on GC electrode with a sweep rate at 5 mV s⁻¹

Figure 4.6b) shows the voltammogram of the Co₃O₄/graphite/Nafion electrode. The spinel Co₃O₄ had 2+ and 3+ oxidation states, which were continuously oxidized on the anodic sweep. In the oxidation scan, there were two distinct peaks at 0.26 and 0.56 V vs. Hg/HgO and then a clear oxygen evolution wave. The oxidation reaction scheme is presented in equations 4.1 and 4.2⁸³, where first spinel cobalt oxide protonation resulted in the cobalt oxyhydroxide phase (Eq. 4.1). Further oxidation produced the cobalt per oxo species (Eq. 4.2), which is highly active for oxygen evolution. On the reduction scan, oxidized species were reduced back in two steps at 0.52 and 0.2 V vs. Hg/HgO related to reduction following redox couples: Co⁴⁺/Co³⁺ and Co³⁺/Co²⁺¹⁰⁷. The oxidized cobalt species were highly active for oxygen evolution reaction^{148, 149}.

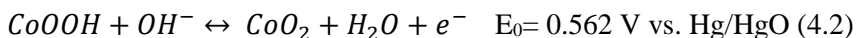
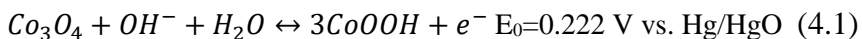


Figure 4.7 shows the CV curve of NiFe sample, heat treated at 250 °C having 0.125 mg cm⁻². There is one well-defined oxidation peak associated with Ni²⁺ to Ni³⁺. After this, there is a broad peak. The redox reaction proceeds in three stages: first, the surface oxidation of Ni to 3+ oxidation state accompanied by hydroxyl ion

intercalation into the interlayer space. At this point, partial charge transfer occurs between Ni and Fe resulting in more positive charge for Ni ¹⁵⁰. In the mixed hydroxide (NiFeOOH), the bond contraction between Fe-O provides the optimum absorption energy for OER intermediate species ¹⁵¹, this reduces the overpotential for the OER. During the second stage, the hydroxide ion is adsorbed by Fe³⁺. Finally, one electron transfer reaction results in oxygen evolution. The underlying oxidation reactions are given in equation (4.3–4.5) ^{152, 153}.

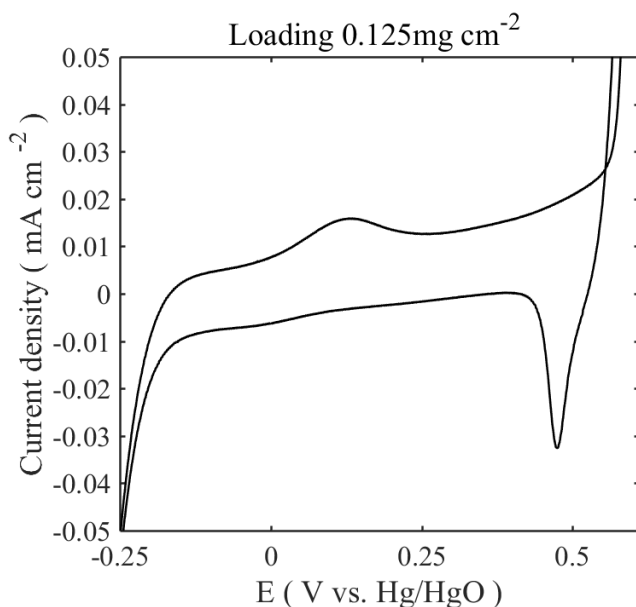
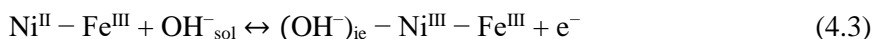


Figure 4.7 CV curve of the NiFe sample at 250 °C on GC electrode at 5mV s⁻¹

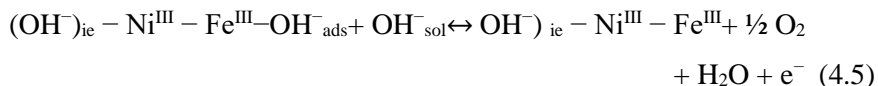
First step (surface oxidation)



Second step (hydroxide adsorption)



Third step (charge transfer)



where, i.e-interlayer species; ads-adsorbate; sol-solution.

XPS results revealed that the NiFe oxide, at 100–250°C, Fe in 3+ state and Ni ions are both in 2+ and 3+ oxidation states, Ni ions are easily oxidizable to oxyhydroxide phases, while Fe^{3+} enhances hydroxide adsorption and thus results in high OER activities.

4.6 Electrode kinetics

4.6.1 Initial stage of the electrocatalytic activity

Figure 4.10 presents the LSV response of LCMO and Co_3O_4 samples with Pt as the reference. The data was corrected for iR and background capacitive current. On the ORR side Pt/C shows the highest current density and the spinel Co_3O_4 has the lowest activity of all the catalysts. The reduction current densities on the ORR side at -0.3 V vs. Hg/HgO, were -2.2, -1.2, -0.97 and -0.3 mA cm^{-2} for Pt, LCMO+ Co_3O_4 , LCMO, and Co_3O_4 , respectively. The LSV profiles show a single sigmoidal shape for Pt and Co_3O_4 , while for LCMO and LCMO+ Co_3O_4 , they show a dual sigmoidal character. These differences in shape might be due to a different oxygen reduction mechanism, depending on either a direct 4 e^- pathway, or indirect 2 e^- pathway, or a combination of both. The OER activities trend were opposite to the ORR and were in the following order: LCMO < Pt/C < LCMO+ Co_3O_4 < Co_3O_4 . Co_3O_4 had the highest activity with 1.3 mA cm^{-2} . The addition of Co_3O_4 resulted in a threefold increase of current density on LCMO from 0.25 to 0.77 mA cm^{-2} . Therefore, the co-catalyst addition improved the bifunctional performances of oxygen electrodes.

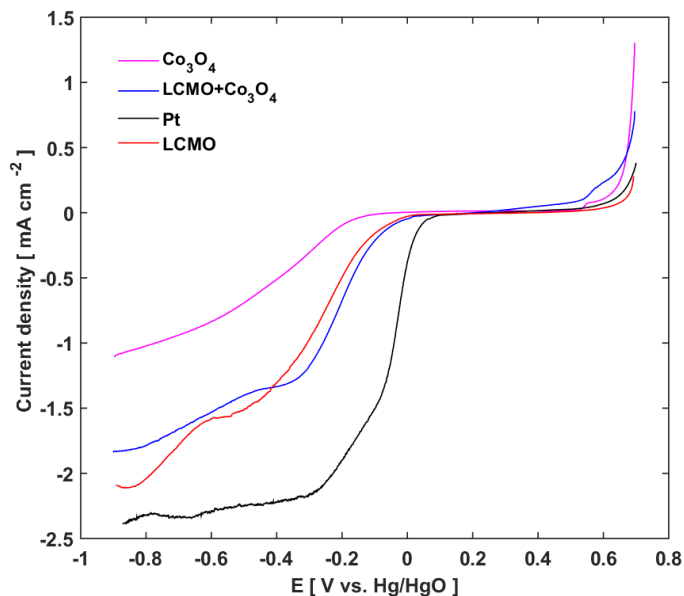


Figure 4.8 LSV response of samples on GC electrode at 5 mV s^{-1} , rotation rate 1600 rpm in O_2 saturated 1M KOH

The linear sweep voltammetries (LSV) of NiFe oxides are shown in Figure 4.9–4.10. Three different catalyst loadings at 0.125, 0.25, and 0.75 mg cm^{-2} were used. The OER activity trends were in the following order, shown in Figure 4.11: $250^\circ\text{C} > 100^\circ\text{C} > 450^\circ\text{C} > 600^\circ\text{C}$ (paper 4). The best one among the various calcination temperatures and loadings was 250°C at 0.125 mg cm^{-2} . The catalyst loading significantly altered the OER activity and onset potential of the different samples. This was due to the catalyst surface morphology, phase, and thickness. As seen in the TEM image in Figure 4.3 a–b, $100\text{--}250^\circ\text{C}$ samples have cavities and edges that are easily exposed to the electrolytes and gas for the OE/OR electrode reaction. However, at $450\text{--}600^\circ\text{C}$, samples tend to agglomerate due to the heat blocking the reaction sites in the samples. Out of the different loadings, the low loadings allowed better metal center accessibility, which resulted in increased OER activity. The highest current density (23 mA cm^{-2} at 0.7 V vs.

Hg/HgO) was observed for a 250 °C sample at 0.125 mg cm⁻². The loadings reduced the current density to 8 and 5 for 0.25 and 0.75 mg cm⁻², respectively.

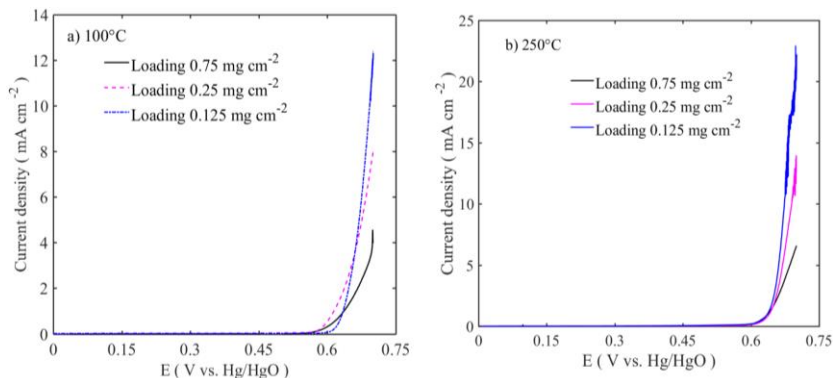


Figure 4.9 OER activity of NiFe oxides (100-250 °C with sweep rate of 5 mV s⁻¹ at 1600 rpm at three different mass loadings .

Figure 4.10 shows the LSV on the ORR side. Here, the catalyst activity is opposite to the OER activity and the loading reduced the ORR activity (onset and current density) (Figure 4.10 a–b). In overall observation, at high temperatures (450 °C and 600 °C) catalysts demonstrated poor performance on both OER and ORR sides due to the reduced number of surface-active sites, phases, surface area, and pore volume. Among the different loadings, the catalyst activity was enhanced on the OER side by the lowest loadings (0.125 mg cm⁻²), while on the ORR side, the highest loadings offered the best activity. The reason for this could be that the thin layer exposed the more active site to the electrolyte, increasing the mass transport of electroactive species and the mass transport of electroactive species. On the other hand, the reaction mechanism was altered on the ORR side due to the conductivity change, depending on the catalyst loading.

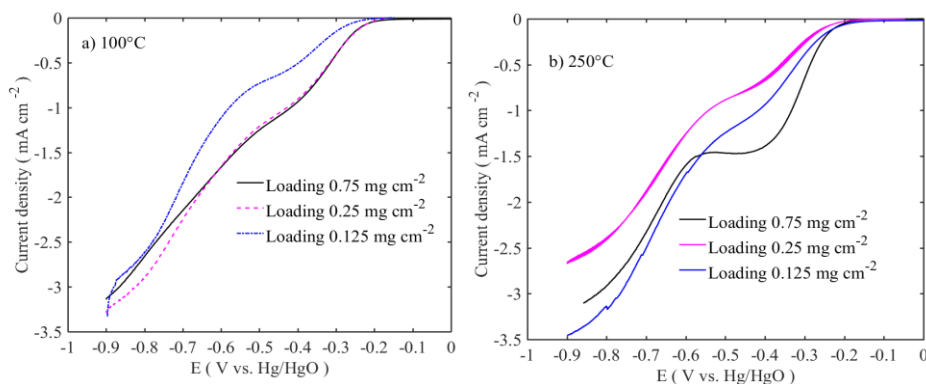


Figure 4.10 ORR activity of NiFe oxides (100-250 °C with sweep rate of 5 mV s^{-1} at 1600 rpm at three different mass loadings.

4.6.2 Tafel characteristics

Tafel analysis was performed to understand the mechanism of the OER and ORR reactions of different catalysts. The Tafel values were extracted from the iR_u and background capacitive current corrected LSV data. The OER Tafel slopes were extracted from the linear part of the curve and for the ORR the slopes were extracted from low and high overpotential regions. The Tafel plots and values of LCMO and Co_3O_4 samples are shown in Table 4.2.

Tafel slopes for the OER side were obtained from Figure 4.10 as follows: 164, 56, 142, and 190 mV decade^{-1} for LCMO, Co_3O_4 , LCMO+ Co_3O_4 and Pt, respectively, from the overpotential region between 0.25 and 0.35 V. These values are in agreement with those reported based manganates and Co_3O_4 literature values^{75, 154}. Based on these values, Pt/C showed poor performance, while Co_3O_4 had very low value (56 mV decade^{-1}), suggesting facile OER kinetics. The Co_3O_4 addition to the LCMO reduced the Tafel slope from 164 to 142 mV decade^{-1} , which is lower than for Pt/C.

The Tafel values for the NiFeO_x samples were calculated from the data in Figures 4.9 and 4.10. The values are shown in Table 4.3. The values were obtained from the potential regions of 0.6 to 0.63 V vs. Hg/HgO. Tafel slope trends were similar to the catalyst activity trend: (39 mV decade^{-1}) $250^\circ\text{C} > 100^\circ\text{C} > 450^\circ\text{C} > 600^\circ\text{C}$ (581 mV

decade⁻¹). Superior activity was exhibited by 250°C, while the 600°C sample demonstrate poor kinetic performance. Another important observation was that catalyst loading increased the Tafel slope values across different calcination temperatures.

The Tafel slope values provide information about the rate determining (RDS) step, surface coverage of adsorbed oxygen species, surface and electronic structures of interphases, and gas bubbles on the surface in the OER/ORR reaction^{155, 156}. For Tafel values closer to 2.3 (2RT/3F)-2.3RT/F such as 39–54 mV decade⁻¹, the O-O bond formation is the RDS, while values greater than this for water adsorption is the RDS¹⁵⁷. Based on this slope value, the Co₃O₄ and NiFe 100–250°C sample has a O-O bond formation as an RDS. However, the other sample LCMO, Pt, the high temperature NiFeO_x are limited by water adsorption as an RDS. Apart from the RDS, low values suggest that the Co₃O₄ and NiFeO_x samples have a mixed valence of metal ion center, giving electrophilic and deprotonating properties, leading to efficient oxygen evolution as shown in the CV image (Figure 4.7) and equation 4.3-4.5. XPS and Raman studies confirmed that the NiFeO_x sample had a varied surface electronic state.

Table 4.2 Tafel characteristics of the LCMO and Co₃O₄

Electrode	Slope (mV decade ⁻¹)		
	OER	ORR Low η	ORR high η
LCMO	164	37	122
Co ₃ O ₄	56	38	119
LCMO+ Co ₃ O ₄	142	28	144
Pt	190	30	128

The ORR Tafel values closer to 30 mV decade⁻¹ at low overpotential and 120 mV decade⁻¹ at the high overpotential region are related to superior kinetics. The ORR Tafel value (28 mV decade⁻¹) of LCMO+Co₃O₄ is closer to the Pt values (30 mV decade⁻¹). These values suggest the superior kinetics of the LCMO materials. The addition of Co₃O₄ did alter the Tafel values slightly. The NiFeO_x Tafel values for low loadings and low temperature at high overpotential are much smaller than the Pt/C. This concurs with the catalytic activity in the previous section as catalyst loading altered the Tafel values. Tafel values did not follow a uniform trend in the NiFeO_x samples.

Table 4.3 Tafel characteristics of the Ni Fe oxide at the different temperatures.

	Tafel Slope (mV Decade ⁻¹)					
	OER			ORR		
Loading (mg cm ⁻²)	0.125	0.25	0.75	0.125	0.25	0.75
100°C	59.1	94.5	98	47	98	126
250°C	39.4	41	54	126	124	84
450°C	70	70	75	95	116	121
600°C	581	461	331	106	81	76

4.7 ORR activity

The RDE experiment was performed to determine the number of electrons transferred during the oxygen reduction reaction (ORR) using the Koutecky-Levich plots. Figures 4.11 and 4.12 show the RDE polarisation curves of LCMO+ Co₃O₄, and NiFeO_x 250°C samples. In all the LCMO and NiFeO_x containing samples, the current-voltage profiles look similar as a bi-sigmoidal shape, which

is due to the ORR mechanism by both $4e^-$ and $2e^-$ pathways contributing to the shape of the polarization curves¹⁵⁸. RDE rotation increases the limiting current density in the samples. The K-L plots of j^{-1} vs. ω^{-1} in most of the samples are linear and parallel to each other at different potentials. This confirms ORR reaction proceeds as first order kinetics.

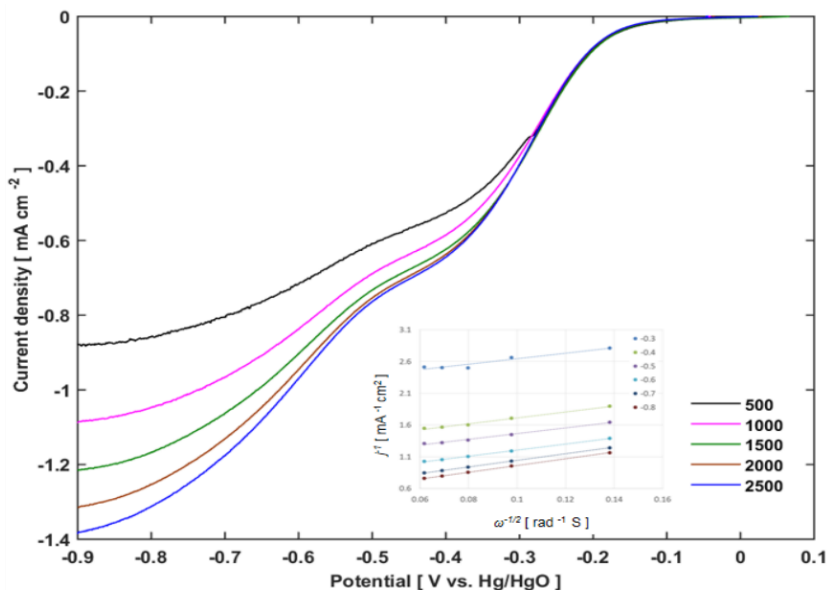


Figure 4.11 RDE curves of LCMO+ Co_3O_4 and its K-L plots placed in the inset figure

The highest limiting currents were observed for 100 °C and 250 °C calcined samples (paper 4) at 0.25 and 0.75 mg.cm^{-2} mass loadings. In these two samples, 100 °C mostly is in LDH phase, while the 250 °C sample both has the spinel and minor other surface sites based on XPS results. The LDH phases performed well due to the small particles, high surface area, and pore volume ($\approx 130 \text{ m}^2 \text{ g}^{-1}$ and $0.80 \text{ cm}^3 \text{ g}^{-1}$), which enhanced the electrocatalytic activity. For other samples at 450–600 °C, the catalyst activity was reduced, due to the lack of different surface oxidation sites and low surface area. On the ORR side, the highest loadings delivered the best performances very

different to the OER activity. This could be due to thin layers enhancing the oxygen mass transport away from the surface, while the thick layer efficiently decomposes the HO_2^- .

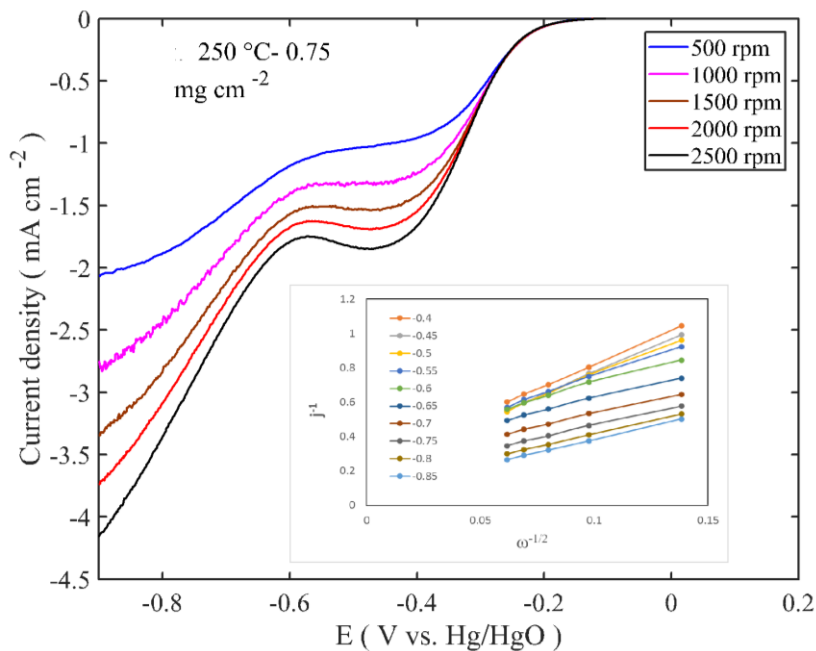


Figure 4.12 RDE curves of 0.75 mg cm^{-2} NiFe samples calcined at different temperatures in 0.1 M KOH with 5 mV s^{-1} at different rotation rates (400–2500 rpm).

Figure 4.13 shows a summary of the number of electrons involved in the ORR. The intrinsic catalytic activity of ORR is directly related to the number of electrons transferred in the ORR reaction. The number of transferred electrons for Co_3O_4 is 1.75 to 2, LCMO and $\text{Co}_3\text{O}_4+\text{LCMO}$ to be 2.75 to 3.2⁷⁶, Pt is 3.6 to 4¹⁵⁹ and the NiFeO_x is 2.5 to 3.5 e^- , which changed based on its potential. The reported number of transferred electrons for the Co_3O_4 -based electrode was 1.75 to 2¹⁶⁰. The Co_3O_4 addition to LCMO maintained the number of electrons involved in ORR at the same level as plain LCMO.

In NiFeO_x samples, 100 °C calcined sample delivered the highest activity (3.4 e⁻ transfer) at 0.75 mg cm⁻², while the 600 °C showed low activity (2.7 e⁻ transfer). Another observation is that the low levels of loadings delivered low intrinsic activity due to the hydrogen peroxide generation¹⁶¹. Overall, the spinel oxides Co₃O₄ and NiFeO_x showed excellent OER properties and the NiFeO_x showed moderate bi-functional activity. LCMO showed high ORR activity. Mixing Co₃O₄ and LCMO resulted in a better performance in both OER/ORR directions.

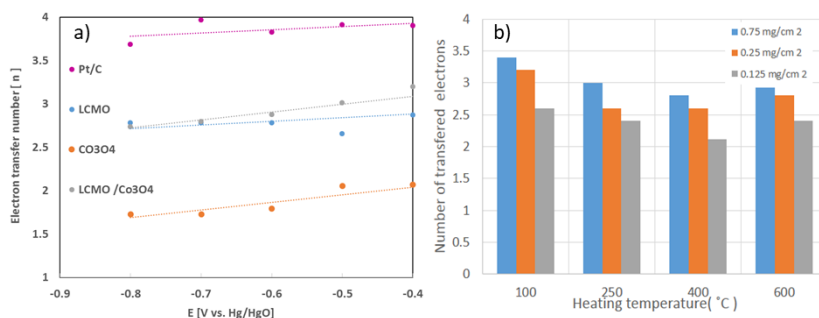


Figure 4.13 Summary of the number of electrons transferred at different potentials on LCMO and Co₃O₄ (a) and NiFe oxide at different temperatures

4.8 Bifunctional OER and ORR cycling

4.8.1 Bifunctional stability of LCMO and Co₃O₄ based electrodes

Bifunctional OER and ORR stability is an important parameter that determines the longevity of the electrode in metal-air battery operation. The electrodes were potentiodynamically cycled at 5 mV s⁻¹ between -0.35 and 0.70 V for the LCMO and Co₃O₄ based gas diffusion electrodes (GDE) and -0.9 to 0.7 V vs. Hg/HgO for NiFeO_x based materials on RDE setup. The electrode compositions and procedures were provided in section 2.3.2 and Table 2.4.

Figure 4.14 (a–d) shows the bifunctional stability of the different catalysts in GDE configuration. The LCMO containing electrode exhibited pseudo capacitive response as shown in the rectangular I-V profiles, which is a common response shown by Mn-based materials due to the electrosorption of K^+ and OH^- ion on the Mn ion oxygen vacancy sites ¹⁶². The LCMO materials showed the initially high current density of 29 mA cm^{-2} for OER and 59 mA cm^{-2} for ORR. At the end of the 50 cycles, these values dropped to 14 and 47 mA cm^{-2} , respectively. Also, the OER profile shifted to 80 mV in a positive direction; both on the OER and ORR direction, the current density decreased. Figure 4.14b shows the cycling response of Co_3O_4 /graphite/GDE. The initial cycles had a 61 and 8 mA cm^{-2} for OER and ORR, respectively. Upon successive cycling (10–50 cycles), the current density improved significantly for the OER to 75 mA cm^{-2} and, for the ORR, increased slightly to 10 mA cm^{-2} . In the Co_3O_4 electrode, both OER and ORR was enhanced by more than 20% on OER, while the ORR current density was more than 7 times lower than the OER. This shows that the LCMO demonstrated better performance on the ORR, while Co_3O_4 performed well on the OER side. Therefore, combining the LCMO and Co_3O_4 catalysts were expected to offer bi-functional OER/ORR performance.

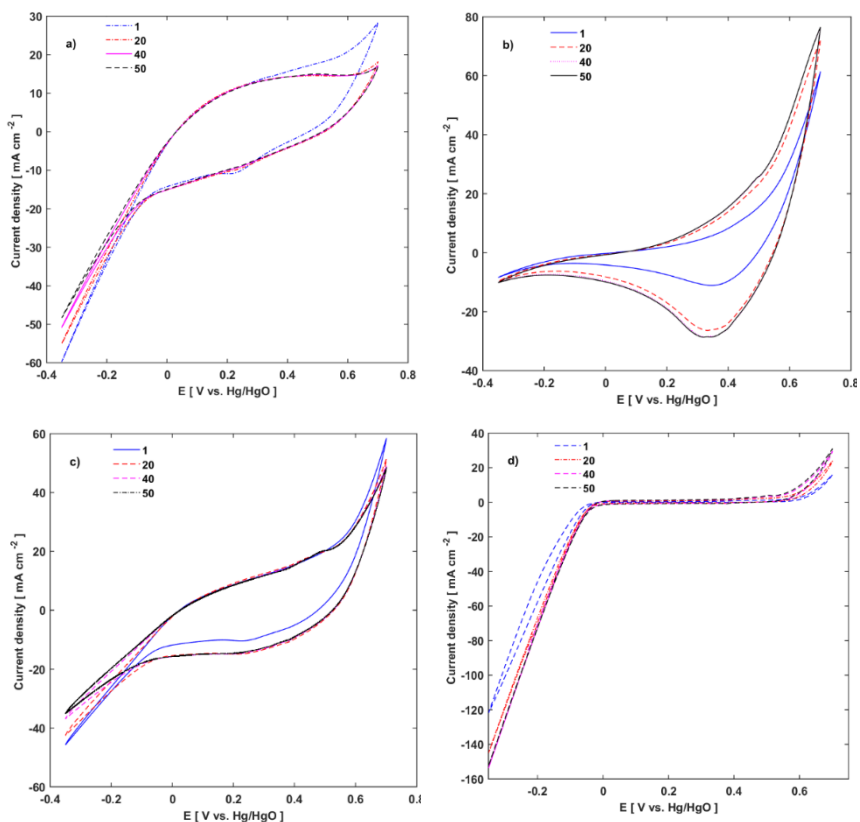


Figure 4.14 Voltammograms for stability tests of the GDEs a) LCMO b) Co₃O₄ c) LCMO+ Co₃O₄ d) Pt/Vulcan XC-72 in O₂ saturated 6M KOH at 5 mV s⁻¹

The LCMO and Co₃O₄ mixed electrode performances are shown in Figure 4.14 c. In the first cycle, the OER and ORR current densities were 58 and 45 mA cm⁻², respectively. After 30 cycles, the performance stabilized, and, finally, at the 50th cycle reached 48 and 37 mA cm⁻². These performance values are comparably higher and constant after an extended 50 cycles than their individual materials. The Co₃O₄ substitution increased the OER performance by a factor of 2 on the LCMO material, while ORR performance reduction was insignificant. The electrode material loadings were 23 and 10 mg cm⁻² for LCMO and Co₃O₄, respectively, while, regarding their

individual electrodes, the loadings were 34 and 32 mg cm⁻². Even though the Co₃O₄ loading in the mixed electrode was lower than its corresponding single oxide electrode, the bifunctional performance was shown to be excellent due to the synergistic combined effects of LCMO and Co₃O₄. The improved performance by the LCMO and Co₃O₄ was due to the physicochemical nature of the spinel and perovskite oxides with their high surface area and interconnected open-pore structure, which was rendered by the synthesis method.

Figure 4.14d shows the OEOR activity of the commercial ETEK 20% Pt on Vulcan XC-72 electrode used as a reference material. As expected, Pt showed the highest oxygen reduction current (120 mA cm⁻²) during the first cycle, which gradually increased to 152 mA cm⁻² on the ORR side, while on the OER showed 31 mA cm⁻² at the 50th cycle, an increase of 16 mA cm⁻² from the initial value. However, the repeated cycles left the electrolyte turn to a brownish color, due to the oxidation of carbon support in the Pt electrode. This was not observed in the other materials of our studies.

4.8.2 Bifunctional stability of NiFeO_x based electrodes

Figures 4.15 exhibit the bifunctional activity of different NiFeO_x samples at different loadings. Among them, the better-performing ones are shown in Figure 4.15. As discussed in earlier section, the 250 °C calcined samples showed higher activity at the OER side in low catalyst loading and for the ORR side, high loading gave a better performance. These trends also followed in the electrochemical stability test (Figure 4.15). The ORR activity trends are similar in all samples (100 – 600 °C) up to 50 cycles with current densities varying between -2.5 and -3.5 mA cm⁻². However, the OER activity was entirely different for calcined samples at different temperatures (paper 4). In the 250 °C calcined sample, OER activity dropped from 21 mA cm⁻² initially to 4 mA cm⁻² at the 50th cycle (Figure 4.15a). At high catalyst loadings (0.25–0.75 mg cm⁻²), OER activity was constant throughout the 50 cycles. The high performance in bifunctional activity by low-temperature samples (100–250 °C) was due to more easily oxidizable Ni ions during the nickel hydroxide/spinel to nickel oxyhydroxide phase. However, in

high-temperature samples (450–600 °C) oxidizable multivalent nickel is not enough to contribute to OER activity, which is also corroborated by the XPS results.

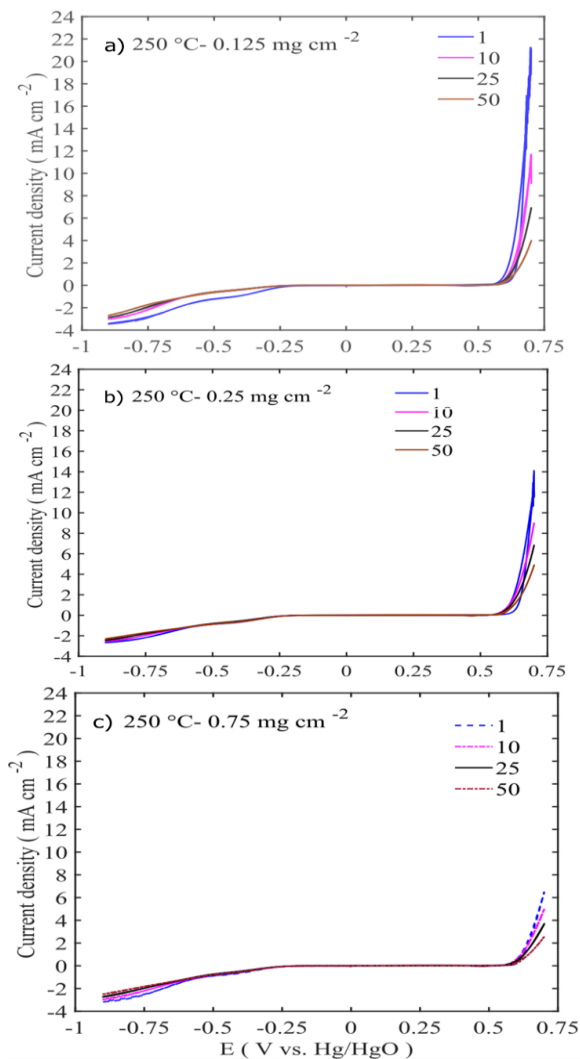


Figure 4.15 Electrochemical stability of NiFe oxide at 250 °C calcined sample with three different mass loadings (a) 0.125, b) 0.25, and c) 0.75 mg cm⁻²

4.9 Mass activity comparison between GC vs. GDE composite electrodes of LCMO+Co₃O₄

The mass activity comparison of GC and GDE electrodes are shown in Figure 4.16. The primary differences between them were the active material loadings, conductivity, hydrodynamic rotation, and binder. The mass loading of GC electrodes was between 0.47 and 0.59 mg cm⁻² and the rotation speed was 1600 rpm. While in the GDE, the mass loading was between 32 and 35 mg cm⁻², and the electrode was stationary. The binder in the GC was nafion, while in the GDE it was PTFE. Comparing all of the results, GC electrodes showed slightly higher mass activity than GDE electrodes, especially on the ORR side. The reason for this could be due to accelerated mass transfer by the thin catalyst layer and rotation. OER mass activities were in the following order: LCMO < LCMO+Co₃O₄ < Co₃O₄, while the ORR was in a reverse trend: LCMO > LCMO+Co₃O₄ > Co₃O₄. It is easy to observe here that Co₃O₄ addition increased OER activity on LCMO, while ORR activity did not change significantly. The Co₃O₄ addition to LCMO increased the activity to 1.3 and -1.98 A g⁻¹ on the OER and ORR side, respectively. The reported perovskite materials in the literature had similar values^{75, 163}.

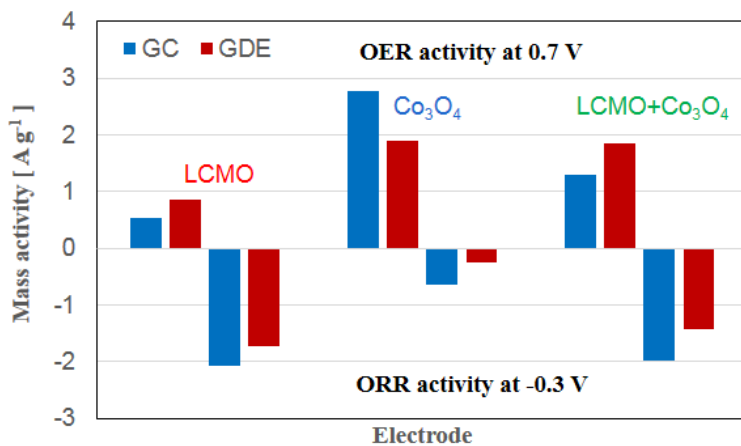


Figure 4.16 Mass activities on the GC and GDE (data extracted from Figure 4.12 and Figure 4.14)

4.10 Postmortem analysis of LCMO and Co₃O₄ cycled electrodes

Figure 4.17 shows the XRD spectra of fresh and cycled electrodes. The fresh Co₃O₄ electrode has the mixture of CoO and Co₃O₄ phases, in which CoO is the reduction product of Co₃O₄ by the sintering condition at 320 °C in the N₂ flow. After 50 cycles of potentiodynamic cycling, it reoxidized the CoO to Co₃O₄ and CoO could no longer be in the diffractograms. In the LCMO-containing material, no extra phases, such as manganese or lanthanum hydroxides and crystallite changes could be detected. This proves that the electrodes are stable during the continuous bifunctional OER/ORR operation.

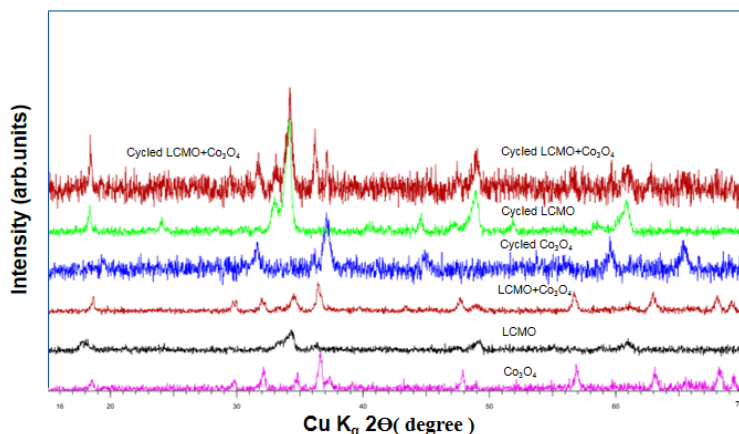


Figure 4.17 XRD patterns of fresh electrodes and after 50 cycles of LCMO and Co_3O_4

The morphological changes of cycled electrodes were observed by SEM as shown in the Figures 4.18. Figures 4.18 presents the surface morphology of the initial cycle (a–b), and, after 50 cycles (c–d) of the LCMO+ Co_3O_4 . After 50 cycles, no significant change was observed; Figure 4.18 (c–d), resembles the initial morphology and size (paper 2). However, the presence of KOH leads to display the roughening of particles (Figure 4.18d). There was no major morphological changes in the samples. This confirms that electrochemical cycling did not alter the surface morphology. Therefore, together with SEM and XRD results, the catalysts are structurally and crystallographically stable for the long-term bifunctional activity of the oxygen electrodes.

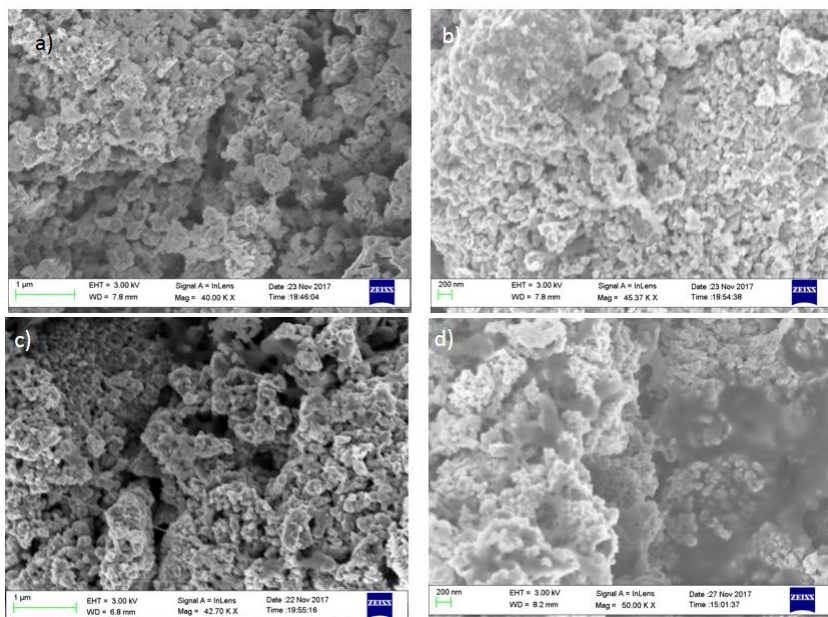


Figure 4.18 Scanning electron microscope pictures LCMO+ Co_3O_4 electrodes at initial (a–b) and after 50 cycles (c–d).

The higher activity exhibited by OER/ORR and durability exhibited by NiFeO_x , LCMO perovskite and spinel Co_3O_4 catalysts mixed together, can offer a noble metal-free, low-cost, earth-abundant bifunctional catalyst for metal-air batteries.

PART IV: FINAL REMARKS

PART IV Final remarks

5 Conclusion and outlook

Cu-doped, CuSn-doped and Sn-doped nano iron active materials were utilized as negative electrodes in alkaline electrolyte for application in Fe-air batteries.

The Cu-doped electrode showed a stable electrode performance of 360 mAh g⁻¹ at 80% charging efficiency; the capacity was even stable at 360 mAh g⁻¹ and also at 500 mA g⁻¹. The Cu presence increased the electrode kinetics in cyclic voltammetry and polarization studies. Impedance analysis shows the increase of surface roughness and reduced ohmic resistance upon cycling. The *ex-situ* cycled electrode's TEM and XRD analysis confirmed that the core shell structure of iron carbide material was intact. Thus, the nanoparticle core-shell structure was preserved.

Among the CuSn- and Sn-doped nano-iron/carbon composites, the CuSn electrode exhibited 470 and 603 mAh g⁻¹ with 91 to 93% charge efficiency upon addition of CNT and LiOH, respectively. The increased charge and discharge performances are due to the Cu, Sn and Fe having been uniformly distributed on the carbon network. Even though the CNT with LiOH additions increased the performance to 91% and 603 mAh g⁻¹, its cycling stability was compromised due to the higher rate of hydrogen evolution, which was confirmed through the *in-operando* MS. There were three distinct hydrogen evolution regions: the first one was less than 1.5 V for the reduction of Fe(OH)₂ to Fe and the least amount of hydrogen; the second region is between 1.5–1.6 V for both iron reduction and constant hydrogen evolution; finally, the higher rate for hydrogen evolution is above 1.65 V. This higher rate of hydrogen evolution at the end of the charge plateau made the electrodes fail rapidly. The different charge current density experiment showed that the charging at high current density increased the charging efficiency and performance, and also reduced the amount of evolved hydrogen due to the current limitation for hydrogen evolution

reaction. These findings will help to develop a suitable charging algorithm in a way to limit the hydrogen evolution for the iron electrode.

The decay in capacity is associated with the disappearance of sulfur from the electrode having Cu and CuSn electrodes, while Sn nano-sized non-uniform particles made the electrodes mechanically unstable. The Cu and CuSn doping made a positive contribution to the electrode performance. However, only Sn doping reduced the performance. This Cu and CuSn nano-iron/carbon composite is a suitable negative electrode for the alkaline Fe-air battery application.

LCMO, Co_3O_4 and NiFeO_x -based non-noble metal catalysts were developed using facile methods. The resultant nanomaterials of both the spinels and the perovskite and LDH phases showed uniform particles with interconnected networks, and high surface and pore volume for the efficient gas-liquid-solid reaction. The heat treatment was used to fine-tune the particle size, phases and surface oxidation states in the NiFeO_x catalyst.

The RDE study of mixed $\text{La}_{0.1}\text{Ca}_{0.9}\text{MnO}_3$ with Co_3O_4 catalyst showed that the optimum performance on the amount of electron transfer was around 3.2 e and this electrode has exhibited superior bi-functional activity and stability for both the ORR and OER. The mass activity performance on GC and GDE was similar on the OER direction, while on the ORR direction there was a minor difference due to electrode composition and rotation. The mass activities of mixed catalysts on the OER and ORR side were found to be 1.3 and 1.98 A g^{-1} , respectively. The high activity of the mixed catalyst could be attributed to the synergistic effect and structural robustness of perovskite and spinel oxides. The cycled GDE electrodes showed a similar phase and structure to fresh electrodes in the *ex-situ* XRD and SEM measurements. The blending of two different catalysts could be a strategy to reduce the high overpotential on OER/ORR.

In the NiFeO_x catalyst materials, the low-temperature treated catalyst (250°C) obtained the highest OER current density as 23 mA

cm^{-2} at 0.7 V and $41 \text{ mV decade}^{-1}$ as the OER Tafel slope, while on the ORR side, the reaction followed a quasi-4 e pathway and had a $124 \text{ mV decade}^{-1}$ of Tafel slope. This higher activity was attributed to a mixed chemical state and heterogeneous distribution of Ni ions in the spinel structure at low temperature as illustrated by XPS. Another important observation is that the catalyst loading changed the activity of the OER/ORR. The thinner catalyst (0.125 mg cm^{-2}) on the OER increased the performance, in contrast to the OER, where a thicker catalyst (0.75 mg cm^{-2}) achieved more electron transfer per oxygen molecule in the ORR.

Bifunctional stability on the ORR side and fairly stable activity on the OER side after 50 cycles was observed. The TEM, XPS and Raman showed elongated-thin nanoparticles with a mixed Ni oxidation state, which further improved the electrocatalytic activity.

The mixing of two different catalysts with nanoparticle approach will help to develop a low-cost electrocatalyst for bifunctional oxygen electrodes for alkaline metal-air batteries.

Future work could be to increase the iron negative electrode life cycles with stable charge efficiency by developing charging algorithms and tuning the capacity utilization to limit the hydrogen evolution and capacity decay. On the air electrode side, bifunctional OER and ORR activity on GDL electrode should be performed with optimum catalyst, highly conductive and stable carbonaceous materials with different additives.

6 Acknowledgment

First of all, I would like to thank my supervisor Docent Yohannes Kiros for his encouragement, support, insights and mentoring me all the way during the studies. I would like to thank Professor Lar Petterson for giving me the opportunity to do my Ph.D in Chemical Engineering.

I would like to extend my gratitude to Fe-air (FAIR) project leaders and colleagues; Professor Dag Noréus, Mylad Chamoun, Dr. Björn Skårman, and Dr. Hilmar Vidarsson, and Dr. Gunder Karlsson for their valuable input and discussions during this thesis work.

I would like to thank Professor Mats Göthelid Dr. Malin. Johansson for their contributions on XPS and Raman studies and Dr. Henrik Svengren for his in-situ GC MS electrochemical studies.

Thanks to all my chemical technology and process technology colleagues and researchers. I also wish to thank the enjoyable time I spent with Zahri, Fatima, Sandra, Jerry, Saiman, Jonas, Pirouz, Jorge, Pouya and Mahmoud and Efthymios. And my special thanks to Fatima, Zahri, Saiman for their gym and Jerry Solis for his restaurant tours.

I would like to thank for the time I spent in overseas during the conference with Hyeyun Kim, Maria, Kevin, Fabian.

I would like to thank my friends outside the department: Sriram, Vigneshwaran, Vali and Alagappan for their valuable suggestions and their support during these years.

I gratefully acknowledge the Swedish Energy Agency (STEM) for the financial support to carry out my Ph.D.

Finally, I would like to thank my family and friends for their endless support, love and encouragement.

7 References

- [1] T. M. Gür *Energy Environ. Sci.* **2018**, *11*, 2696-2767.
- [2] U. E. P. Agency. **2017**, Nov 10, 2017.
- [3] Global Wind Energy Council, Global Wind 2015 Report: Annual Market Update, April **2016**
- [4] S. R. Narayanan, G. K. S. Prakash, A. Manohar, B. Yang, S. Malkhandi, A. Kindler *Solid State Ionics.* **2012**, *216*, 105-109.
- [5] H. Ibrahim, A. Ilinca, J. Perron *Renewable and Sustainable Energy Reviews.* **2008**, *12*, 1221-1250.
- [6] I. Hadjipaschalis, A. Poullikkas, V. Efthimiou *Renewable and Sustainable Energy Reviews.* **2009**, *13*, 1513-1522.
- [7] S. Vazquez, S. M. Lukic, E. Galvan, L. G. Franquelo, J. M. Carrasco *IEEE Transactions on Industrial Electronics.* **2010**, *57*, 3881-3895.
- [8] A. Castillo, D. F. Gayme *Energ Convers Manage.* **2014**, *87*, 885-894.
- [9] D. O. Akinyele, R. K. Rayudu *Sustainable Energy Technologies and Assessments.* **2014**, *8*, 74-91.
- [10] H. Chen, T. N. Cong, W. Yang, C. Tan, Y. Li, Y. Ding *Progress in Natural Science.* **2009**, *19*, 291-312.
- [11] D. Larcher, J. M. Tarascon *Nat Chem.* **2015**, *7*, 19-29.
- [12] M. K. Ravikumar, S. Rathod, N. Jaiswal, S. Patil, A. Shukla *Journal of Solid State Electrochemistry.* **2016**, 1-22.
- [13] D. Linden, T. B. Reddy, Handbook of batteries, New York : McGraw-Hill, New York, **2002**.
- [14] K. Vijayamohanan, T. S. Balasubramanian, A. K. Shukla *Journal of Power Sources.* **1991**, *34*, 269-285.
- [15] A. H. Abdalla, C. I. Oseghale, J. O. G. Posada, P. J. Hall, IET Renewable Power Generation, **2016**, *10*, 1529-1534.
- [16] M. S. Whittingham *Proceedings of the IEEE.* **2012**, *100*, 1518-1534.
- [17] B. Dunn, H. Kamath, J.-M. Tarascon *Science.* **2011**, *334*, 928-935.
- [18] M. Yekini Suberu, M. Wazir Mustafa, N. Bashir *Renewable and Sustainable Energy Reviews.* **2014**, *35*, 499-514.

- [19] Y. Li, J. Lu *ACS Energy Letters*. **2017**, 2, 1370-1377.
- [20] US Geological Survey, Mineral Commodity Summaries, Jan. **2016**.
- [21] S. Malkhandi, B. Yang, A. K. Manohar, G. K. S. Prakash, S. R. Narayanan *Journal of the American Chemical Society*. **2012**, 135, 347-353.
- [22] Y. Gorlin, T. F. Jaramillo *Journal of the American Chemical Society*. **2010**, 132, 13612-13614.
- [23] A. R. Paulraj, Y. Kiros *Journal of Solid State Electrochemistry*. **2018**.
- [24] W. Song, Z. Ren, S.-Y. Chen, Y. Meng, S. Biswas, P. Nandi, H. A. Elsen, P.-X. Gao, S. L. Suib *ACS Applied Materials & Interfaces*. **2016**, 8, 20802-20813.
- [25] L. Jörissen *J Power Sources*. **2006**, 155, 23-32.
- [26] K. Vijayamohanan, A. K. Shukla, S. Sathyanarayana *Journal of Power Sources*. **1987**, 21, 53-57.
- [27] A. K. Manohar, C. Yang, S. Malkhandi, B. Yang, G. K. Surya Prakash, S. R. Narayanan *Journal of The Electrochemical Society*. **2012**, 159, A2148-A2155.
- [28] A. K. Manohar, C. Yang, S. R. Narayanan *Journal of The Electrochemical Society*. **2015**, 162, A1864-A1872.
- [29] R. D. McKerracher, C. Ponce de Leon, R. G. A. Wills, A. A. Shah, F. C. Walsh *ChemPlusChem*. **2015**, 80, 323-335.
- [30] H. Osgood, S. V. Devaguptapu, H. Xu, J. Cho, G. Wu *Nano Today*. **2016**, 11, 601-625.
- [31] R. D. McKerracher, C. P. d. Leon, R. G. A. Wills, A. A. Shah, F. C. Walsh *ChemPlusChem*. **2015**, 80, 323-335.
- [32] L. Öjefors *Journal of The Electrochemical Society*. **1976**, 123, 1691-1696.
- [33] B. Andersson, L. Öjefors *Journal of The Electrochemical Society*. **1976**, 123, 824-828.
- [34] N. Jayalakshmi, V. S. Muralidharan *Journal of Power Sources*. **1990**, 32, 277-286.
- [35] G. P. Kalaignan, V. S. Muralidharan, K. I. Vasu *J Appl Electrochem*. **1987**, 17, 1083-1092.

- [36] M. K. Ravikumar, A. S. Rajan, S. Sampath, K. R. Priolkar, A. K. Shukla *Journal of The Electrochemical Society*. **2015**, 162, A2339-A2350.
- [37] K. Vijayamohanan, A. K. Shukla, S. Sathyanarayana *Journal of Power Sources*. **1990**, 32, 329-339.
- [38] R. Carta, S. Dernini, A. M. Polcaro, P. F. Ricci, G. Tola, , *Journal of Electroanalytical Chemistry*, **1988**, 251, 257-268.
- [39] I. Flis-Kabulska, J. Flis *International Journal of Hydrogen Energy*. **2014**, 39, 3597-3605.
- [40] L. Öjefors *Electrochimica Acta*. **1976**, 21, 263-266.
- [41] J. Černý, K. Micka *Journal of Power Sources*. **1989**, 25, 111-122.
- [42] P. R. Vassie, A. C. C. Tseung *Electrochimica Acta*. **1976**, 21, 299-302.
- [43] D. Lei, D. C. Lee, A. Magasinski, E. Zhao, D. Steingart, G. Yushin *ACS Appl Mater Interfaces*. **2016**, 8, 2088-2096.
- [44] W. Jiang, F. Liang, J. Wang, L. Su, Y. Wu, L. Wang *Rsc Adv*. **2014**, 4, 15394-15399.
- [45] A. Ito, L. Zhao, S. Okada, J.-i. Yamaki *Journal of Power Sources*. **2011**, 196, 8154-8159.
- [46] E. Shangguan, L. Guo, F. Li, Q. Wang, J. Li, Q. Li, Z. Chang, X.-Z. Yuan *Journal of Power Sources*. **2016**, 327, 187-195.
- [47] E. Shangguan, F. Li, J. Li, Z. Chang, Q. Li, X.-Z. Yuan, H. Wang *Journal of Power Sources*. **2015**, 291, 29-39.
- [48] B. T. Hang, T. Watanabe, M. Eashira, I. Watanabe, S. Okada, J.-i. Yamaki *Electrochemical and Solid-State Letters*. **2005**, 8, A476-A480.
- [49] B. T. Hang, T. Watanabe, M. Eashira, S. Okada, J.-i. Yamaki, S. Hata, S.-H. Yoon, I. Mochida *Journal of Power Sources*. **2005**, 150, 261-271.
- [50] B. T. Hang, M. Eashira, I. Watanabe, S. Okada, J.-I. Yamaki, S.-H. Yoon, I. Mochida *Journal of Power Sources*. **2005**, 143, 256-264.
- [51] C. Y. Kao, K. S. Chou *Journal of Power Sources*. **2010**, 195, 2399-2404.

- [52] D. Lei, D.-C. Lee, A. Magasinski, E. Zhao, D. Steingart, G. Yushin *ACS Applied Materials & Interfaces*. **2016**, 8, 2088-2096.
- [53] T. Kim, Y. Ohata, J. Kim, C. K. Rhee, J. Miyawaki, S.-H. Yoon *Carbon*. **2014**, 80, 698-707.
- [54] K.-C. Huang, K.-S. Chou *Electrochemistry Communications*. **2007**, 9, 1907-1912.
- [55] C. X. Guo, C. M. Li *Nano Energy*. **2017**, 42, 166-172.
- [56] X. Wu, H. B. Wu, W. Xiong, Z. Le, F. Sun, F. Liu, J. Chen, Z. Zhu, Y. Lu *Nano Energy*. **2016**, 30, 217-224.
- [57] A. S. Rajan, S. Sampath, A. K. Shukla *Energy Environ. Sci.* **2014**, 7, 1110-1116.
- [58] C.-Y. Kao, Y.-R. Tsai, K.-S. Chou *J Power Sources*. **2011**, 196, 5746-5750.
- [59] M. Chamoun, B. Skårman, H. Vidarsson, R. I. Smith, S. Hull, M. Lelis, D. Milcius, D. Noréus *Journal of The Electrochemical Society*. **2017**, 164, A1251-A1257.
- [60] Y. Li, H. Dai *Chemical Society Reviews*. **2014**, 43, 5257-5275.
- [61] Y. Lee, J. Suntivich, K. J. May, E. E. Perry, Y. Shao-Horn *The Journal of Physical Chemistry Letters*. **2012**, 3, 399-404.
- [62] J. Chen, B. Lim, E. P. Lee, Y. Xia *Nano Today*. **2009**, 4, 81-95.
- [63] A. Morozan, B. Josselme, S. Palacin *Energy Environ. Sci.* **2011**, 4, 1238-1254.
- [64] R. D. McKerracher, C. Alegre, V. Baglio, A. S. Aricò, C. Ponce de León, F. Mornaghini, M. Rodlert, F. C. Walsh *Electrochimica Acta*. **2015**, 174, 508-515.
- [65] D. Chen, C. Chen, Z. M. Baiyee, Z. Shao, F. Ciucci *Chemical Reviews*. **2015**, 115, 9869-9921.
- [66] X. Li, W. Qu, J. Zhang, H. Wang *Journal of The Electrochemical Society*. **2011**, 158, A597-A604.
- [67] H. Zhu, P. Zhang, S. Dai *ACS Catalysis*. **2015**, 5, 6370-6385.
- [68] J. Sunarso, A. A. J. Torriero, W. Zhou, P. C. Howlett, M. Forsyth *The Journal of Physical Chemistry C*. **2012**, 116, 5827-5834.
- [69] J. Suntivich, K. J. May, H. A. Gasteiger, J. B. Goodenough, Y. Shao-Horn *Science*. **2011**, 334, 1383-1385.

- [70] J. Suntivich, H. A. Gasteiger, N. Yabuuchi, H. Nakanishi, J. B. Goodenough, Y. Shao-Horn *Nat Chem.* **2011**, 3, 647-647.
- [71] W. T. Hong, M. Risch, K. A. Stoerzinger, A. Grimaud, J. Suntivich, Y. Shao-Horn *Energy Environ. Sci.* **2015**, 8, 1404-1427.
- [72] M. S. D. Read, M. Saiful Islam, G. W. Watson, F. King, F. E. Hancock *Journal of Materials Chemistry.* **2000**, 10, 2298-2305.
- [73] Y. Liu, J. Dong, D. Y. Xing *Eur. Phys. J. B.* **1998**, 3, 185-188.
- [74] X. Han, T. Zhang, J. Du, F. Cheng, J. Chen *Chemical Science.* **2013**, 4, 368-376.
- [75] J. Kim, X. Yin, K.-C. Tsao, S. Fang, H. Yang *Journal of the American Chemical Society.* **2014**, 136, 14646-14649.
- [76] V. Celorrio, L. Calvillo, E. Dann, G. Granozzi, A. Aguadero, D. Kramer, A. E. Russell, D. J. Fermin *Catalysis Science & Technology.* **2016**, 6, 7231-7238.
- [77] M. Bursell, M. Pirjamali, Y. Kiros *Electrochimica Acta.* **2002**, 47, 1651-1660.
- [78] H. Morimoto, M. Kamata, T. Esaka *Journal of The Electrochemical Society.* **1996**, 143, 567-570.
- [79] H. Morimoto, T. Esaka, S. Takai *Materials Research Bulletin.* **1997**, 32, 1359-1366.
- [80] G. Karlsson *Electrochimica Acta.* **1985**, 30, 1555-1561.
- [81] Y. Yan, B. Y. Xia, B. Zhao, X. Wang *J Mater Chem A.* **2016**, 4, 17587-17603.
- [82] N. N. Binitha, P. V. Suraja, Z. Yaakob, M. R. Resmi, P. P. Siliya *J Sol-Gel Sci Techn.* **2010**, 53, 466-469.
- [83] T. Meng, Q.-Q. Xu, Z.-H. Wang, Y.-T. Li, Z.-M. Gao, X.-Y. Xing, T.-Z. Ren *Electrochimica Acta.* **2015**, 180, 104-111.
- [84] S. Zhao, B. Rasimick, W. Mustain, H. Xu *Applied Catalysis B: Environmental.* **2017**, 203, 138-145.
- [85] Y. Huang, M. Zhang, P. Liu, L. Wang, F. Cheng *Ionics.* **2016**, 1-8.
- [86] S. K. Singh, V. M. Dhavale, S. Kurungot *ACS Applied Materials & Interfaces.* **2015**, 7, 21138-21149.
- [87] R. Ramsundar, J. Debgupta, V. Pillai, P. Joy *Electrocatalysis.* **2015**, 6, 331-340.

- [88] H. M. A. Amin, H. Baltruschat, D. Wittmaier, K. A. Friedrich *Electrochimica Acta*. **2015**, *151*, 332-339.
- [89] M. Aghazadeh *J Appl Electrochem*. **2012**, *42*, 89-94.
- [90] W. Liu, H. Yang, L. Zhao, S. Liu, H. Wang, S. Chen *Electrochimica Acta*. **2016**, *207*, 293-300.
- [91] A. J. Esswein, M. J. McMurdo, P. N. Ross, A. T. Bell, T. D. Tilley *The Journal of Physical Chemistry C*. **2009**, *113*, 15068-15072.
- [92] Y. Liang, Y. Li, H. Wang, J. Zhou, J. Wang, T. Regier, H. Dai *Nat Mater*. **2011**, *10*, 780-786.
- [93] J. Jiang, W. Shi, S. Song, Q. Hao, W. Fan, X. Xia, X. Zhang, Q. Wang, C. liu, D. Yan *Journal of Power Sources*. **2014**, *248*, 1281-1289.
- [94] X. W. Lou, D. Deng, J. Y. Lee, J. Feng, L. A. Archer *Advanced Materials*. **2008**, *20*, 258-262.
- [95] D. Wittmaier, S. Aisenbrey, N. Wagner, K. A. Friedrich *Electrochimica Acta*. **2014**, *149*, 355-363.
- [96] Z. Song, Y. Zhang, W. Liu, S. Zhang, G. Liu, H. Chen, J. Qiu *Electrochimica Acta*. **2013**, *112*, 120-126.
- [97] J. Xu, P. Gao, T. S. Zhao *Energy Environ. Sci*. **2012**, *5*, 5333-5339.
- [98] M. De Koninck, S.-C. Poirier, B. Marsan *Journal of The Electrochemical Society*. **2007**, *154*, A381-A388.
- [99] D. U. Lee, B. J. Kim, Z. Chen *J Mater Chem A*. **2013**, *1*, 4754-4762.
- [100] Y. Liang, H. Wang, J. Zhou, Y. Li, J. Wang, T. Regier, H. Dai *Journal of the American Chemical Society*. **2012**, *134*, 3517-3523.
- [101] S. Trasatti *Journal of Electroanalytical Chemistry and Interfacial Electrochemistry*. **1980**, *111*, 125-131.
- [102] P. H. Benhangi, A. Alfantazi, E. Gyenge *Electrochimica Acta*. **2014**, *123*, 42-50.
- [103] S. Anantharaj, K. Karthick, M. Venkatesh, T. V. S. V. Simha, A. S. Salunke, L. Ma, H. Liang, S. Kundu *Nano Energy*.
- [104] S. Anantharaj, K. Karthick, S. Kundu *Materials Today Energy*. **2017**, *6*, 1-26.

- [105] L. Trotochaud, S. L. Young, J. K. Ranney, S. W. Boettcher *Journal of the American Chemical Society*. **2014**, *136*, 6744-6753.
- [106] D. A. Corrigan *Journal of The Electrochemical Society*. **1987**, *134*, 377-384.
- [107] M. Hamdani, R. Singh, P. Chartier *Int. J. Electrochem. Sci.* **2010**, *5*, 556.
- [108] L. Hu, L. Wu, M. Liao, X. Hu, X. Fang *Advanced Functional Materials*. **2012**, *22*, 998-1004.
- [109] N.-L. Wu, W.-R. Liu, S.-J. Su *Electrochimica Acta*. **2003**, *48*, 1567-1571.
- [110] R. Cao, J.-S. Lee, M. Liu, J. Cho *Advanced Energy Materials*. **2012**, *2*, 816-829.
- [111] E. L. Miller, R. E. Rocheleau *Journal of The Electrochemical Society*. **1997**, *144*, 3072-3077.
- [112] Y. Vlamidis, E. Scavetta, M. Gazzano, D. Tonelli *Electrochimica Acta*. **2016**, *188*, 653-660.
- [113] J. Du, C. Chen, F. Cheng, J. Chen *Inorganic Chemistry*. **2015**, *54*, 5467-5474.
- [114] C. Yuan, H. B. Wu, Y. Xie, X. W. Lou *Angewandte Chemie International Edition*. **2014**, *53*, 1488-1504.
- [115] F. Cheng, J. Shen, B. Peng, Y. Pan, Z. Tao, J. Chen *Nature Chemistry*. **2010**, *3*, 79.
- [116] M. E. G. Lyons, R. L. Doyle, M. P. Browne, I. J. Godwin, A. A. S. Rovetta *Current Opinion in Electrochemistry*. **2017**, *1*, 40-45.
- [117] M. Srivastava, S. Chaubey, A. K. Ojha *Materials Chemistry and Physics*. **2009**, *118*, 174-180.
- [118] P. Dolcet, S. Diodati, F. Zorzi, P. Voepel, C. Seitz, B. Smarsly, S. Mascotto, F. Nestola, S. Gross *Green Chemistry*. **2018**.
- [119] A. Paulraj, Y. Kiros, M. Göthelid, M. Johansson *Catalysts*. **2018**, *8*, 328.
- [120] T. S. Balasubramanian, A. K. Shukla *Journal of Power Sources*. **1993**, *41*, 99-105.
- [121] H. Svengren, M. Chamoun, J. Grins, M. Johnsson *ChemElectroChem*. **2018**, *5*, 44-50.
- [122] F. Li, Y. Pan, H. Wang, X. Huang, Q. Zhang, Z. Peng, Y. Tang *Journal of The Electrochemical Society*. **2017**, *164*, A1333-A1338.

- [123] B. Wang, T. Liu, A. Liu, G. Liu, L. Wang, T. Gao, D. Wang, X. S. Zhao *Advanced Energy Materials*. **2016**, 6, 1600426.
- [124] R. Li, Y. Wang, C. Zhou, C. Wang, X. Ba, Y. Li, X. Huang, J. Liu *Advanced Functional Materials*. **2015**, 25, 5384-5394.
- [125] V. Ciupina, G. Prodan, F. Dumitrache, I. Morjan, R. Alexandrescu, E. Popovici, I. Soare, L. Albu, R. Birjega, B. David, O. Schneeweiss *Proceedings SPIE 5924, Complex Mediums VI: Light and Complexity*, 592418 (23 August **2005**).
- [126] F. Li, E. Shangguan, J. Li, L. Li, J. Yang, Z. Chang, Q. Li, X.-Z. Yuan, H. Wang *Electrochimica Acta*. **2015**, 178, 34-44.
- [127] A. Annamalai, P. S. Shinde, T. H. Jeon, H. H. Lee, H. G. Kim, W. Choi, J. S. Jang *Solar Energy Materials and Solar Cells*. **2016**, 144, 247-255.
- [128] K. Xie, Z. Lu, H. Huang, W. Lu, Y. Lai, J. Li, L. Zhou, Y. Liu *Journal of Materials Chemistry*. **2012**, 22, 5560-5567.
- [129] L. Bokobza, J.-L. Bruneel, M. Couzi *C*. **2015**, 1, 77.
- [130] K.-H. Wu, D.-W. Wang, D.-S. Su *ChemElectroChem*. **2016**, n/a-n/a.
- [131] G. Valyulene, A. Zhelene, V. Jasulaitene, B. Shimkunaite *Russian Journal of Applied Chemistry*. **2007**, 80, 1322-1326.
- [132] B. T. Hang, D. H. Thang *J Alloy Compd*. **2016**, 655, 44-49.
- [133] B. T. Hang, S. H. Yoon, S. Okada, J. Yamaki *Journal of Power Sources*. **2007**, 168, 522-532.
- [134] B. T. Hang, T. Watanabe, M. Egashira, I. Watanabe, O. Shigeto, J. Yamaki *Journal of Power Sources*. **2006**, 155, 461-469.
- [135] K. Vijayamohanan, A. K. Shukia, S. Sathyanarayana *Journal of Electroanalytical Chemistry and Interfacial Electrochemistry*. **1990**, 289, 55-68.
- [136] K. Vijayamohanan, A. K. Shukla, S. Sathyanarayana *Journal of Electroanalytical Chemistry and Interfacial Electrochemistry*. **1990**, 295, 59-70.
- [137] B. Wang, Y. Xie, T. Liu, H. Luo, B. Wang, C. Wang, L. Wang, D. Wang, S. Dou, Y. Zhou *Nano Energy*. **2017**, 42, 363-372.
- [138] B. Wang, W. Al Abdulla, D. Wang, X. S. Zhao *Energy Environ. Sci*. **2015**, 8, 869-875.

- [139] A. R. Paulraj, Y. Kiros, B. Skårman, H. Vidarsson *Journal of The Electrochemical Society*. **2017**, *164*, A1665-A1672.
- [140] B. Yang, S. Malkhandi, A. K. Manohar, G. K. S. Prakash, S. R. Narayanan *Energy Environ. Sci.* **2014**, *7*, 2753-2763.
- [141] K. C. Huang, K. S. Chou *Electrochemistry Communications*. **2007**, *9*, 1907-1912.
- [142] C. Lucas, I. Eiroa, M. R. Nunes, P. A. Russo, M. M. L. Ribeiro Carrott, M. I. da Silva Pereira, M. E. Melo Jorge *Journal of Solid State Electrochemistry*. **2009**, *13*, 943-950.
- [143] J. Du, T. Zhang, F. Cheng, W. Chu, Z. Wu, J. Chen *Inorganic Chemistry*. **2014**, *53*, 9106-9114.
- [144] M. Prabu, K. Ketpang, S. Shanmugam *Nanoscale*. **2014**, *6*, 3173-3181.
- [145] M. Soldemo, E. Lundgren, J. Weissenrieder *Surf Sci.* **2016**, *644*, 172-179.
- [146] T. Yamashita, P. Hayes *Applied Surface Science*. **2008**, *254*, 2441-2449.
- [147] G. H. Jaffari, A. K. Rumaiz, J. C. Woicik, S. I. Shah *J Appl Phys.* **2012**, *111*, 093906.
- [148] S. Palmas, F. Ferrara, A. Vacca, M. Mascia, A. M. Polcaro *Electrochimica Acta*. **2007**, *53*, 400-406.
- [149] S. Palmas, F. Ferrara, A. Pisu, C. Cannas *Chemical Papers*. **2007**, *61*, 77-82.
- [150] Q. Zhao, J. Yang, M. Liu, R. Wang, G. Zhang, H. Wang, H. Tang, C. Liu, Z. Mei, H. Chen, F. Pan *ACS Catalysis*. **2018**, 5621-5629.
- [151] S. Klaus, Y. Cai, M. W. Louie, L. Trotochaud, A. T. Bell *The Journal of Physical Chemistry C*. **2015**, *119*, 7243-7254.
- [152] M. A. Oliver-Tolentino, J. Vázquez-Samperio, A. Manzo-Robledo, R. d. G. González-Huerta, J. L. Flores-Moreno, D. Ramírez-Rosales, A. Guzmán-Vargas *The Journal of Physical Chemistry C*. **2014**, *118*, 22432-22438.
- [153] E. B. Castro, C. A. Gervasi *International Journal of Hydrogen Energy*. **2000**, *25*, 1163-1170.
- [154] M. E. Lyons, M. P. Brandon *Int. J. Electrochem. Sci.* **2008**, *3*, 1386-1424.

- [155] J. O. Bockris, T. Otagawa *The Journal of Physical Chemistry*. **1983**, 87, 2960-2971.
- [156] P. Hosseini-Benhangi, M. A. Garcia-Contreras, A. Alfantazi, E. L. Gyenge *Journal of The Electrochemical Society*. **2015**, 162, F1356-F1366.
- [157] T. A. C., C. E. B., S. S. L., A. N. H., M. I. G., F. Laszlo, B. Eric, K. Qing, R. R. C., K. M. L., Z. M. J., S. D. R. *Angewandte Chemie International Edition*. **2016**, 55, 10381-10385.
- [158] J. Tulloch, S. W. Donne *Journal of Power Sources*. **2009**, 188, 359-366.
- [159] Y. J. Sa, K. Kwon, J. Y. Cheon, F. Kleitz, S. H. Joo *J Mater Chem A*. **2013**, 1, 9992-10001.
- [160] P. Thangasamy, K. Selvakumar, M. Sathish, S. M. S. Kumar, R. Thangamuthu *Catalysis Science & Technology*. **2017**, 7, 1227-1234.
- [161] G. Zhang, Q. Wei, X. Yang, A. C. Tavares, S. Sun *Applied Catalysis B: Environmental*. **2017**, 206, 115-126.
- [162] J. T. Mefford, W. G. Hardin, S. Dai, K. P. Johnston, K. J. Stevenson *Nat Mater*. **2014**, 13, 726-732.
- [163] K. Nishio, S. Molla, T. Okugaki, S. Nakanishi, I. Nitta, Y. Kotani *Journal of Power Sources*. **2015**, 278, 645-651.